

RESEARCH ARTICLE

EXIT-Chart Aided Design of Irregular Multiple-Rate Quantum Turbo Block Codes

DARYUS CHANDRA, SOON XIN NG[✉], (Senior Member, IEEE),
AND LAJOS HANZO[✉], (Life Fellow, IEEE)

School of Electronics and Computer Science, University of Southampton, SO17 1BJ Southampton, U.K.

Corresponding author: Lajos Hanzo (lh@soton.ac.uk)

The work of Lajos Hanzo was supported in part by the Engineering and Physical Sciences Research Council under Project EP/W016605/1, Project EP/X01228X/1, and Project EP/Y026721/1; and in part by the European Research Council's Advanced Fellow Grant QuantCom under Grant 789028.

ABSTRACT We propose a novel quantum turbo short-block code, which subsumes multiple-rate quantum short-block codes (MR-QSBCs) as the outer codes and a quantum unity-rate code (QURC) as the inner code. The proposed design is denoted as MR-QSBC-QURC. More specifically, the proposed design exhibits multiple quantum coding rates despite relying only on a single quantum encoder. Moreover, the flexibility offered by the single-encoder MR-QSBCs enables us to leverage extrinsic information transfer (EXIT)-chart based heuristic optimization for determining the optimal weighting in the fractional encoding of MR-QSBCs. Our simulation results show that the MR-QSBC-QURC scheme conceived performs relatively close to the ultimate limit of the quantum hashing bound. Specifically, when considering the target quantum coding rates of $r_Q = \{0.3, 0.4, 0.5, 0.6, 0.7\}$, the MR-QSBC-QURC operates at a distance of $D = \{0.042, 0.029, 0.030, 0.024, 0.017\}$ from the quantum hashing bound, respectively, at a quantum bit error ratio (QBER) of 10^{-3} .

INDEX TERMS Quantum error-correction codes, quantum stabilizer codes, quantum turbo codes, quantum short-block codes, EXIT chart, rate-compatible code.

I. INTRODUCTION

Quantum error-correction codes (QECCs) [1], [2], [3] constitute a potent technique of mitigating the deleterious effects of quantum decoherence that is prevalent in quantum systems [4], [5]. The conception of quantum stabilizer codes (QSCs) [6] has triggered a massive redesign of classical correction codes for their application in the quantum realm. Consequently, the “quantumization” of powerful classical error correction codes [7], [8], [9], [10] leads to the emergence of novel classes of QSCs, such as quantum polar codes (QPCs) [11], [12], quantum low-density parity-check (LDPC) codes [13], [14], as well as quantum turbo codes (QTCs) [15], [16]. However, classical error-correction codes cannot be directly transplanted into the quantum domain, since they have to satisfy the stringent requirement of the so called symplectic criterion [3], [17]. This challenge becomes particularly pronounced when attempting to design

a broad class of QSCs capable of adapting their error correction capability to the quality of quantum channels. Explicitly, when the quality of the quantum channel starts degrading, a QSC operating beyond its quantum error correction capability may actually introduce more errors instead of correcting them. Thus, we may reduce the quantum coding rate of the QSC by incorporating more redundancy qubits. Similarly, when the quality of the quantum channel starts improving, we may increase the quantum coding rate accordingly to reduce the number of redundancy qubits for the sake of improving the effective throughput of the QSC. However, the well-established classical methods such as puncturing and extending the mother code often do not satisfy the stringent symplectic criterion imposed in quantum domain [18], [19]. Therefore, a novel design paradigm has to be conceived for designing adaptive and rate-compatible QSCs.

The seminal family of rate-compatible QTCs was conceived in [16], [20] by employing quantum irregular convolutional codes (QIrCCs) as the inner and outer codes.

The associate editor coordinating the review of this manuscript and approving it for publication was Majed Haddad[✉].

Unfortunately, the subcomponent QIRCCs proposed cannot be created from a single mother code. Hence, the implementation of QIRCCs requires a different quantum encoder for each subcomponent code. Furthermore, since it relies on fractional encoding of the subcomponent codes, a number of the subcomponent quantum encoders have to be prepared. Subsequently, another design was proposed in [21], namely the QIRCC-QURC, where the inner codes previously constituted by QIRCCs were replaced by a quantum unity-rate code (QURC). The QURC was employed as the inner code, iteratively exchanging information with the QIRCCs serving as the outer codes, while maintaining the quantum coding rate. In this particular scheme, since the fractional irregular encoding operations are only performed by the outer codes, the number of quantum encoders required for the entire scheme can be substantially reduced. More recently, an alternative QTC scheme was proposed in [22], where the outer codes are constructed by quantum short-block codes (QSBC). While the QSBCs conceived successfully accommodate a wide range of quantum coding rates as the outer codes, the proposed design only covers the quantum coding rates of $r_Q \geq 0.5$. Additionally, the outer codes were not optimized, despite having the potential of performing fractional encoding using single-encoder-based multiple-rate quantum short-block codes (MR-QSBCs).

The design of near-capacity QTCs based on optimal fractional subcomponent codes may be achieved by invoking extrinsic information transfer (EXIT)-chart based heuristic optimization [16], [20], [21], [23], [24], [25], [26], [27], [28]. Explicitly, a near-capacity operation may be attained for any arbitrary coding rate by optimizing the weighting factors of the subcomponent codes. In the conventional near-capacity QTCs, the subcomponent codes having various quantum coding rates will be represented by different quantum encoders. However, in this treatise, we envisage the attractive solution where a carefully designed quantum encoder can be used to accommodate subcomponent codes having a wide-range quantum coding rates. Therefore, we firmly believe that the benefit of EXIT-chart based optimization can be fully exploited when the subcomponent codes can be represented by a single encoder, which has not been achieved by any QTC construction.

Against this background, we conceive a *single encoder that fits all* types of QECCs as our main contribution in this treatise. More specifically, our contributions may be summarized as follows:

- We formulate and characterize the family of single-encoder MR-QSBCs, where only a single quantum encoder is required for supporting a wide-range of quantum coding rates suitable for different quantum depolarizing probabilities.
- We design single-encoder-based multiple-rate quantum turbo short-block codes by concatenating single-encoder MR-QSBCs with a QURC. We refer to this design as MR-QSBC-QURC.

- We perform heuristic EXIT-chart based optimization for designing our optimal MR-QSBC-QURC. Despite relying on low-complexity MR-QSBCs as the outer codes, they provide a near-hashing bound performance. Specifically, the quantum bit error ratio (QBER) of our half-rate MR-QSBC-QURC is comparable to that of the best-performing half-rate QTCs in the open literature, namely the QIRCC-QURC of [21].
- Finally, our proposed scheme performs very close to the quantum hashing bound for a wide range of quantum coding rates, while maintaining a QBER of 10^{-3} .

The rest of this treatise is organized as follows. In Section II, we present the proposed MR-QSBCs and demonstrate that they can be constructed using only a single quantum encoder for a wide range of quantum coding rates. In Section III, we amalgamate MR-QSBCs and a QURC for constructing multiple-rate QTCs, which we refer to as MR-QSBC-QURC. The step-by-step optimization of the MR-QSBCs using the EXIT-chart based heuristic search is given in Section IV. We evaluate the performance of the optimized MR-QSBC-QURCs in terms of their QBER, performance gaps with the quantum hashing bound as well as goodput for various quantum coding rates in Section V. Finally, we conclude and summarize our design guidelines in Section VI, while highlighting some potential future research directions.

II. QUANTUM SHORT-BLOCK CODES (QSBCs)

The classical short-block codes (SBCs) are binary systematic linear block codes $\mathcal{C}(n, k, d)$, whose generator matrix \mathbf{G} is defined by

$$\mathbf{G} = [\mathbf{I}_k | \mathbf{P}_{k,(n-k)}] = [\mathbf{I}_k | \mathbf{1}_{k,1}], \quad (1)$$

for $k < n$, where k is the length of the original information word, n is the length of the encoded codeword, \mathbf{I}_k is a k -dimension identity matrix, $\mathbf{P}_{k,(n-k)}$ is a $[k \times (n - k)]$ -element binary matrix, and $\mathbf{1}_{m,n}$ is a $(m \times n)$ -element all-one matrix. The parity-check matrix (PCM) \mathbf{H} of a systematic linear block code is formulated as $\mathbf{H} = [\mathbf{P}^T | \mathbf{I}_{n-k}]$. Therefore, the PCM \mathbf{H} of the classical SBCs is given by

$$\mathbf{H} = \mathbf{1}_{1,n}, \quad (2)$$

which is an all-one $(1 \times n)$ -element matrix. Finally, the resultant classical coding rate r_C is given by

$$r_C = \frac{k}{n} = \frac{n-1}{n}, \quad (3)$$

for $n \geq 2$. The minimum distance of the SBCs conceived is $d = 2$, which implies that classical SBCs constitute a family of single-error detection codes. Having said that, the minimum distance $d = 2$ guarantees the convergence of iterative decoding to a vanishingly low BER, when they are employed as the outer code within a concatenated coding scheme [29], [30].

By exploiting the classical-to-quantum isomorphism [31], the classical SBCs whose PCM is specified in (2) can be

readily transformed into their quantum counterparts. Given a pair of classical codes $\mathcal{C}_1(n, k_1, d_1)$ and $\mathcal{C}_2(n, k_2, d_2)$ having PCMs of \mathbf{H}_1 and \mathbf{H}_2 , respectively, a quantum stabilizer code (QSC) $\mathcal{C}[N, K, D]$ ¹ having a binary PCM \mathbf{H} can be constructed by having $\mathbf{H}_x = \mathbf{H}_1$ and $\mathbf{H}_z = \mathbf{H}_2$, where \mathbf{H}_x is used for mitigating the bit-flip (X) errors and \mathbf{H}_z is used for mitigating the phase-flip errors (Z) of quantum Pauli channels. Given a pair of PCMs \mathbf{H}_x and \mathbf{H}_z , we may construct a Calderbank-Shor-Steane (CSS)-type QSC, whose binary PCM \mathbf{H} is defined as follows [2], [32]:

$$\mathbf{H} = \left[\begin{array}{c|c} \mathbf{H}_z & \mathbf{0} \\ \mathbf{0} & \mathbf{H}_x \end{array} \right]. \quad (4)$$

Thus, the code parameters of the resultant CSS-type QSC are constrained by the parameters of the classical constituent codes. More specifically, we have $N = n$, $K = k_1 + k_2 - n$, and $D = \min(d_1, d_2)$. In order to conceive a valid PCM \mathbf{H} for a CSS-type QSC, a pair of PCMs \mathbf{H}_x and \mathbf{H}_z has to satisfy the following symplectic criterion [17], [33]:

$$\mathbf{H}_z \mathbf{H}_x^T = 0. \quad (5)$$

A specific case of CSS-type QSCs associated with $\mathbf{H}_x = \mathbf{H}_z$ may be referred to as dual-containing CSS-type QSCs. Therefore, the PCM \mathbf{H} of dual-containing CSS-type QSCs derived from the classical SBCs of (2) is given by the following definition.

Definition 1 (QSBCs Type-I [22]): QSBCs obtained from the classical PCM of (2) resulting in the following PCM of dual-containing CSS-type QSCs:

$$\mathbf{H} = \left[\begin{array}{c|c} \mathbf{1}_{1,n} & \mathbf{0} \\ \mathbf{0} & \mathbf{1}_{1,n} \end{array} \right], \quad (6)$$

where $n \geq 2$ is an even number – which automatically satisfies the symplectic criterion of (5)– are referred to as quantum short-block codes (QSBCs) Type-I [22].

For a dual-containing CSS-type QSC, the relationship between the classical coding rate of $r_C = k/n$ and its quantum coding rate counterpart of $r_Q = K/N$ can be described explicitly as follows [3], [16], [34]:

$$r_Q = 2r_C - 1. \quad (7)$$

Since the quantum coding rate r_Q has to be positive ($r_Q > 0$), the classical mother codes must exhibit a classical coding rate of $r_C > 1/2$. Consequently, the quantum coding rate r_Q of the QSBCs Type-I can be immediately expressed as

$$r_Q = \frac{N - 2}{N}, \quad (8)$$

for any even number of $N > 2$.

Remark 1: The classical SBCs of $\mathcal{C}(n, k, d) = \mathcal{C}(n, n - 1, 2)$ can be readily transformed into QSBCs Type-I of $\mathcal{C}[N, K, D] = \mathcal{C}[n, n - 2, 2]$ for any even number of $n > 2$.

¹To avoid confusion, we use the notation of $\mathcal{C}(n, k, d)$ for denoting classical error-correction codes and $\mathcal{C}[N, K, D]$ for quantum error-correction codes. For classical error-correction codes, n is the length of the codeword, k is the length of the information word, and the d is the minimum distance of the classical code. Meanwhile, for quantum error correction codes, N is the number of physical/encoded qubits, K is the number of logical/information qubits, and D is the minimum distance of the quantum code.

TABLE 1. The syndrome value evaluation of a single bit-flip error using the QSBC Type-I having the stabilizer generators provided in Example 1.

Error (e)	Syndrome (s)	Error Detection
IIIIIX	1	Yes
IIII XI	1	Yes
IIIXII	1	Yes
II XIII	1	Yes
IXIIII	1	Yes
XIIIII	1	Yes

Example 1: For $n = 6$, we obtain a QSBC Type-I of $\mathcal{C}[N, K, D] = [6, 4, 2]$ having the stabilizer generators of $\mathcal{S} = \{\mathbf{XXXXXX}, \mathbf{ZZZZZZ}\}$. The syndrome value evaluation for a single bit-flip (X) error is given in Table 1. The syndrome value evaluation for a single phase-flip error (Z) is identical to that of a single bit-flip error, since QSBCs of Type-I belong to the family of dual-containing CSS-type QSCs.

We employed the method of constructing dual-containing CSS-type QSCs encoder \mathcal{V} presented in [13], [22], and [35] to design the QSBCs Type-I encoder \mathcal{V} as portrayed in Fig. 1.² The quantum encoder of any QSC may be constructed using the quantum gates constituted by quantum Clifford gates. Furthermore, the quantum encoder MR-QSBCs advocated in this treatise can be constructed using only Hadamard (H)³ and controlled-NOT (CNOT) gates. Specifically, Fig. 1(a) depicts the QSBC $\mathcal{C}[4, 2, 2]$ encoder \mathcal{V} , which is identical to that presented in [37]. By incorporating additional quantum gates and connections denoted by the blue dashed lines in the encoder \mathcal{V} of Fig. 1(b) into the encoder \mathcal{V} of Fig. 1(a), we obtain the QSBC $\mathcal{C}[6, 4, 2]$ encoder \mathcal{V} . Similarly, by adding the quantum gates and connections denoted by red dashed-dotted lines to the encoder \mathcal{V} of Fig. 1(b), we can readily create the QSBC $\mathcal{C}[8, 6, 2]$ encoder \mathcal{V} . Demonstratively, we have constructed QSBCs Type-I encoder \mathcal{V} having a higher quantum coding rate that simultaneously contains the quantum encoder \mathcal{V} exhibiting lower quantum coding rates. Consequently, it is not necessary to construct more than a single encoder \mathcal{V} for various quantum coding rates of QSBCs Type-I since the QSBCs encoder \mathcal{V} exhibits a self-contained structure.

It is important to highlight that this appealing feature is reminiscent of the classical rate-compatible punctured coding philosophy proposed in [38], where the redundant part of the codeword may be flexibly punctured to obtain a higher-rate classical code. Therefore, the mother code should be designed very carefully so that the punctured version of the code will inherit the desired error correction properties.

²In this treatise, our emphasis is on designing the quantum encoder \mathcal{V} for dual-containing CSS-type QSCs. For readers who might like to delve deeper into the general construction of the quantum encoder \mathcal{V} , including non-CSS QSCs, we recommend the paper by Cleve and Gottesman [36].

³In Fig. 1(a), the notation H represents Hadamard gate and not parity-check matrix H .

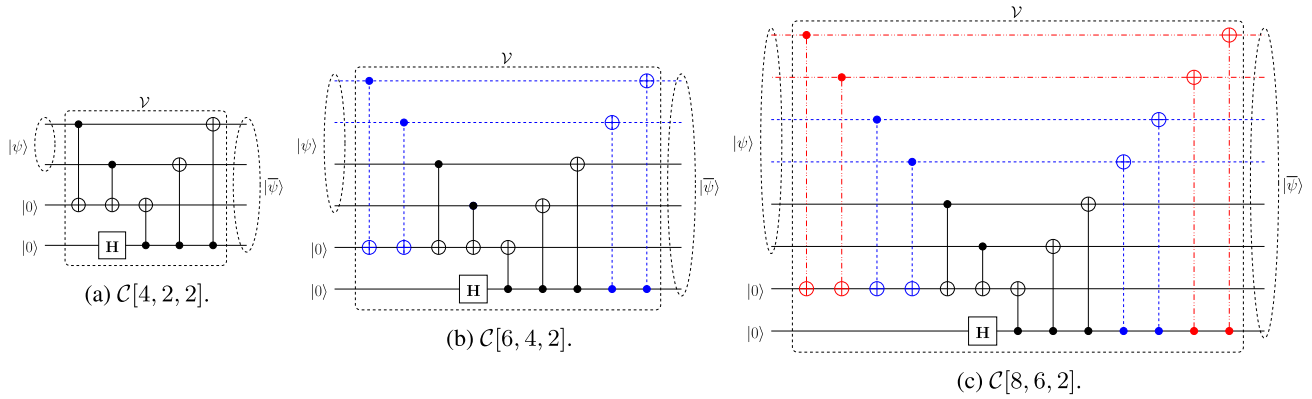


FIGURE 1. The QSBs Type-I encoder \mathcal{V} for quantum coding rates of $r_Q = \{1/2, 2/3, 3/4\}$ illustrating the flexibility and scalability of the code constructions.

As we can observe, the multiple-rate QSBs Type-I encoder \mathcal{V} of Fig. 1 is only scalable for $r_Q \geq 0.5$. Therefore, in addition to the QSBs Type-I, we propose a novel family of QSBs, whose quantum encoder exhibits the capability of accommodating multiple quantum coding rates of $r_Q \leq 0.5$. The proposed QSBs are obtained based on classical SBCs having the systematic generator matrix $G = [I_k | P_{k, (n-k)}]$, where the matrix P^T is given by $P^T = [\mathbf{1}_{(n-k), (2k-n)} | I_{n-k}]$ for $2k > n$. Therefore, the PCM H of this particular family of classical SBCs assumes a systematic form given by

$$H = [\mathbf{1}_{(n-k), (2k-n)} | I_{n-k} | I_{n-k}]. \tag{9}$$

The PCM of the classical SBCs in (9) automatically satisfies the symplectic criterion for even numbers n . The resultant classical SBCs also exhibit the minimum distance of $d \geq 2$, which is lower-bounded by the row-weight of the generator matrix G . Finally, the PCM H of dual-containing CSS-type QSBs derived from the classical SBCs of (9) is given by the following definition.

Definition 2 (QSBs Type-II): QSBs obtained from the classical PCM of (9) resulting in the following PCM of dual-containing CSS-type QSBs:

$$H = \begin{bmatrix} \mathbf{1}_{(n-k), (2k-n)} | I_{n-k} | I_{n-k} & \mathbf{0} \\ \mathbf{0} & \mathbf{1}_{(n-k), (2k-n)} | I_{n-k} | I_{n-k} \end{bmatrix}, \tag{10}$$

where $n \geq 2$ is an even number and $k = \frac{1}{2}(n + 2)$ – which automatically satisfying the symplectic criterion of (5) – are referred to as quantum short-block codes (QSBs) Type-II.

Therefore, the quantum coding rate r_Q of the resultant QSBs Type-II can be explicitly expressed as

$$r_Q = \frac{2}{N}, \tag{11}$$

for any even number of $N > 2$.

Remark 2: The classical SBCs of $C(n, k, d) = C(n, \frac{1}{2}(n + 2), 2)$ can be readily transformed into QSBs Type-II of $C[N, K, D] = C[n, 2, 2]$ for any even number of $n > 2$.

TABLE 2. The syndrome vector evaluation of a single bit-flip error using the QSB Type-II having the stabilizer generators provided in Example 2.

Error e	Syndrome (s_1, s_2)	Error Detection
<i>IIIIIX</i>	(0 1)	Yes
<i>IIIIXI</i>	(1 0)	Yes
<i>IIIXII</i>	(0 1)	Yes
<i>IIIXIII</i>	(1 0)	Yes
<i>IXIIII</i>	(1 1)	Yes
<i>XIIIII</i>	(1 1)	Yes

Example 2: For $n = 6$, we obtain a QSB Type-II of $C[N, K, D] = [6, 2, 2]$ having the stabilizer generators of $S = \{XXIXIX, XXXIXI, ZZIZIZ, ZZZIZI\}$. The syndrome vector evaluation for a single bit-flip (X) error is given in Table 2. The syndrome vector evaluation for a single phase-flip error (Z) is identical to that of a single bit-flip error, since QSBs Type-II belong to the family of dual-containing CSS-type QSBs.

Similarly, by following the method of constructing encoder \mathcal{V} presented in [13], [22], and [35] and based on the PCM H of (9), we obtain the multiple-rate QSBs Type-II encoder \mathcal{V} having the number of physical qubits $N = \{4, 6, 8\}$, as shown in Fig. 2. More explicitly, Fig. 2(a) depicts the QSB $C[4, 2, 2]$ encoder \mathcal{V} , which is identical to the encoder \mathcal{V} of Fig. 1(a). Similar to Fig. 1, the encoder \mathcal{V} of Fig. 2(a) can be transformed into the QSB $C[6, 2, 2]$ encoder \mathcal{V} of Fig. 2(b) by adding the quantum gates and connections denoted by blue dashed lines and into the QSB $C[8, 2, 2]$ encoder \mathcal{V} of Fig. 2(c) by incorporating the quantum gates and connections denoted by red dashed-dotted lines.

Remark 3: The quantum encoders \mathcal{V} portrayed in Fig. 1 and 2 can be combined into a single encoder \mathcal{V} . Ultimately, we have successfully amalgamated QSBs exhibiting a wide-range quantum coding rates r_Q into a single quantum encoder \mathcal{V} . We refer to this joint code constructions as multiple-rate quantum short-block codes (MR-QSBs).

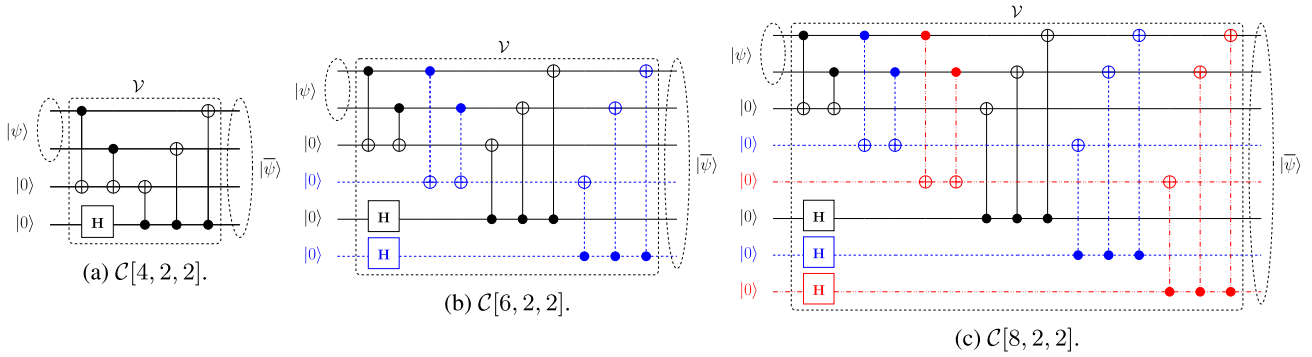


FIGURE 2. The quantum encoders \mathcal{V} of QSBC type-II for quantum coding rates of $r_Q = \{1/2, 1/3, 1/4\}$ illustrating the flexibility and scalability of the code constructions.

III. QUANTUM TURBO SHORT-BLOCK CODES

A. CONCATENATED CODE DESIGN

The resultant MR-QSBCs exhibit the minimum distance of $d = 2$, which means that they only have the error-detection capability and no error-correction capability. To transform this error-detection capability into an error-correction one, we may serially concatenate the MR-QSBCs with a quantum unity-rate code (QURC). This serial concatenation scheme provides us with two main benefits. Firstly, this allows us to employ an iterative turbo decoding between MR-QSBCs as the outer codes and a QURC used as the inner code. Secondly, we do not sacrifice the quantum coding rate of the MR-QSBCs as the outer codes since the QURC does not reduce the throughput [21], [22]. In the following subsections, we will elaborate on the detailed operation of the resultant multiple-rate quantum turbo short-block codes (MR-QSBC-QURC). We commence with the encoding process, followed by the quantum depolarizing channel model, and finally, the decoding process. The general schematic of the proposed MR-QSBC-QURC scheme is portrayed in Fig. 3.

B. ENCODING PROCESS

The encoding process is initiated by the outer quantum encoder \mathcal{V}_1 of Fig. 3, which is constituted by MR-QSBC encoders. This first step maps K_1 logical qubits into N_1 encoded physical qubits with the aid of $(N_1 - K_1)$ auxiliary qubits, which can be formally expressed as

$$\mathcal{V}_1 \left(|\psi\rangle^{K_1} \otimes |0\rangle^{\otimes(N_1-K_1)} \right) = |\overline{\psi}_1\rangle^{N_1}. \quad (12)$$

The output of \mathcal{V}_1 is then fed into the interleaver Π of Fig. 3, which can be represented as a permutation matrix formulated as

$$\Pi \left(|\overline{\psi}_1\rangle^{N_1} \right) = |\psi_2\rangle^{K_2}, \quad (13)$$

where we have $K_2 = N_1$. The interleaver does not modify the number of physical qubits, since it only rearranges the qubit indices within the encoded state of the physical qubits. In this treatise, we utilize random interleaver noting that there are different interleaver types available in the literature [39].

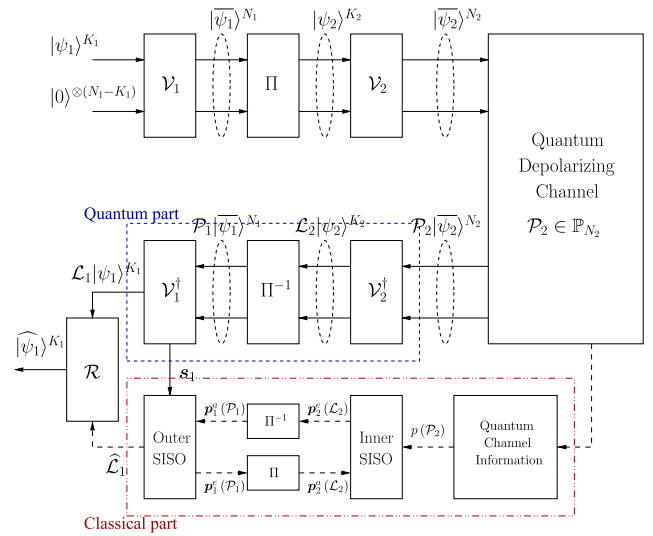


FIGURE 3. The general schematic of the proposed MR-QSBC-QURC scheme.

Next, the output of the interleaver Π is fed into the inner encoder \mathcal{V}_2 , which carries out the following transformation:

$$\mathcal{V}_2 \left(|\psi\rangle^{K_2} \otimes |0\rangle^{\otimes(N_2-K_2)} \right) = |\overline{\psi}_2\rangle^{N_2}. \quad (14)$$

The encoder \mathcal{V}_2 of Fig. 3 maps the state of K_2 logical qubits into the state of N_2 physical qubits with the aid of $(N_2 - K_2)$ auxiliary qubits. Here, we employ the QURC as our inner code. Therefore, the transformation in (14) can be simplified as follows:

$$\mathcal{V}_2 \left(|\psi\rangle^{K_2} \right) = |\overline{\psi}_2\rangle^{N_2}, \quad (15)$$

where $K_2 = N_2$. Finally, the physical qubits exhibiting the quantum state $|\overline{\psi}_2\rangle^{N_2}$ are sent through the quantum channel.

C. QUANTUM DEPOLARIZING CHANNEL

In this treatise, we rely on the quantum depolarizing channel [40], which is a special type of quantum Pauli channels popularly used for modelling the quantum decoherence. Accordingly, the quantum channel is modelled by a quantum

error operator \mathcal{P}_2 , which is represented by the N_2 -tuple Pauli operator ($\mathcal{P}_2 \in \mathbb{P}_{N_2}$). The action of the error operator \mathcal{P}_2 on the encoded state of physical qubits $|\overline{\psi}_2\rangle^{N_2}$ can be formulated as

$$|\widehat{\psi}\rangle^{N_2} = \mathcal{P}_2 \left(|\overline{\psi}_2\rangle^{N_2} \right), \quad (16)$$

where the error operator \mathcal{P}_2 is characterized by the depolarizing probability p . More specifically, each qubit may independently experience a bit-flip (X) error, a phase-flip (Z) error as well as a simultaneous bit-flip and phase-flip (Y) error. The probability that each qubit is experiencing an X , Z , and Y error is denoted by p_x , p_z , and p_y , respectively. Here, we assume that $p_x + p_z + p_y = p$ and $p_x = p_z = p_y = p/3$ [40]. Nonetheless, we can extend the assumption to the asymmetric scenario of $p_x \neq p_z \neq p_y$, which can be deemed to be more realistic based on the physical implementation [41]. However, choosing the value such as $p_x = p_z = p_y$ provides us with the worst-case scenario for quantum Pauli channels, because we have to provide an identical level of protection for different types of errors without favoring only one specific type of error, which may result in quantum coding rate or QBER improvements. For a more detailed discourse on QTCs designed for asymmetric quantum Pauli channels, we refer the enthusiastic readers to [41].

D. DECODING PROCESS

The decoding of MR-QSBC-QURC utilizes the same iterative decoding principle as the conventional QTCs. Specifically, it can be separated into two main parts, namely the classical part and the quantum part. As shown in Fig. 3, the quantum part is denoted by all the components bounded by the blue dashed lines and the classical part is denoted by all the components bounded by the red dashed-dotted lines. Let us first commence by describing the quantum part of the MR-QSBC-QURC decoding.

1) QUANTUM PART

For MR-QSBC-QURC, the quantum-domain operations of Fig. 3 are commenced by the inverse encoder \mathcal{V}_2^\dagger that performs the following transformation on the corrupted quantum state of the physical qubits:

$$\mathcal{V}_2^\dagger(|\widehat{\psi}\rangle^{N_2}) = \mathcal{V}_2^\dagger \left(\mathcal{P}_2 |\overline{\psi}_2\rangle^{N_2} \right) = \mathcal{L}_2 |\psi_2\rangle^{K_2} \otimes \mathcal{S}_2 |0\rangle^{\otimes(N_2-K_2)}. \quad (17)$$

The inverse encoder \mathcal{V}_2^\dagger has a strong resemblance of the quantum encoder \mathcal{V}_2 since they are constituted by an identical quantum circuit apart from the reversed input and output qubits. Observe in (17) that the act of the inverse encoder \mathcal{V}_2^\dagger on the Pauli error operator \mathcal{P}_2 is the decomposition of \mathcal{P}_2 into two Pauli operator components. The first component is \mathcal{L}_2 , which is the logical error operator potentially corrupting the K_2 logical qubits, and the second component is \mathcal{S}_2 , which is the error operator applied to the $(N_2 - K_2)$ auxiliary qubits. The measurement of the erroneous auxiliary qubits

$\mathcal{S}_2 |0\rangle^{N_2-K_2}$ results in the classical bits s_2 , which are fed into the classical part of the iterative decoder. For any MR-QSBC-QURC, the outer inverse encoder \mathcal{V}_2^\dagger is constituted by the inverse encoder of QURC, and therefore we have $N_2 = K_2$. Consequently, the expression of (17) can be further simplified to

$$\mathcal{V}_2^\dagger \left(\mathcal{P}_2 |\overline{\psi}_2\rangle^{N_2} \right) = \mathcal{L}_2 |\psi_2\rangle^{K_2}. \quad (18)$$

Next, the output of the inverse encoder \mathcal{V}_2^\dagger is passed through the deinterleaver Π^{-1} , which performs the following transformation:

$$\Pi^{-1}(\mathcal{L}_2 |\psi_2\rangle^{K_2}) = \mathcal{P}_1 |\overline{\psi}_1\rangle^{N_1}. \quad (19)$$

The output of the deinterleaver is then fed into the quantum inverse encoder \mathcal{V}_1^\dagger , which carries out the following transformation:

$$\mathcal{V}_1^\dagger(\mathcal{P}_1 |\overline{\psi}_1\rangle^{N_1}) = \mathcal{L}_1 |\psi_1\rangle^{K_1} \otimes \mathcal{S}_1 |0\rangle^{\otimes(N_1-K_1)}. \quad (20)$$

Similar to the action of inverse encoder \mathcal{V}_2^\dagger , the inverse encoder \mathcal{V}_1^\dagger also performs a decomposition of the Pauli error operator \mathcal{P}_1 into two components, namely the \mathcal{L}_1 and \mathcal{S}_1 . More specifically, \mathcal{L}_1 is the logical error operator potentially corrupting the K_1 logical qubits and \mathcal{S}_1 is the error operator applied to the $(N_1 - K_1)$ auxiliary qubits.

In MR-QSBC-QURC, the inverse encoder \mathcal{V}_1^\dagger is constituted by the inverse encoders of MR-QSBCs, which is described by the conjugate transpose of the encoder \mathcal{V}_1 . The measurement of the erroneous auxiliary qubits $\mathcal{S}_1 |0\rangle^{N_1-K_1}$ results in classical bits of s_1 , which are equivalent to the classical syndrome values. These syndrome values are then fed into the classical part of the iterative decoder. Finally, based on the result obtained from the classical part of the iterative decoding, an error recovery operator \mathcal{R} is applied to the output of the inverse encoder \mathcal{V}_1^\dagger , which can be described as follows:

$$\mathcal{R} \left(\mathcal{L}_1 |\psi_1\rangle^{K_1} \right) = |\widehat{\psi}_1\rangle^{K_1}. \quad (21)$$

If $\mathcal{R} = \mathcal{L}_1$, we obtain $|\widehat{\psi}_1\rangle^{K_1} = |\psi_1\rangle^{K_1}$, which completes our decoding process.

2) CLASSICAL PART

For MR-QSBC-QURC, the classical-domain operations of Fig. 3 are started by obtaining the information about the depolarizing probability p of the quantum depolarizing channel associated with the error operator \mathcal{P}_2 . We assume that the MR-QSBC-QURC decoder has perfect knowledge of depolarizing probability p , which is acceptable since an online depolarizing probability estimator based on syndrome measurements tailored for QTC has been proposed recently in [42]. Additionally, the QBER performance of QTCs in the range of low depolarizing probability values is rather insensitive to the depolarizing probability estimation [43].

In summary, based on the classical syndrome s_1 and on the depolarizing probability p , the pair of classical soft-input and

soft-output (SISO) decoders of Fig. 3 aim for determining the most likely error coset $\widehat{\mathcal{L}}_1$ imposed on the logical qubits $|\psi_1\rangle^{K_1}$. Formally, this can be written as a maximum *a posteriori* (MAP) decoding as follows [16], [20]:

$$\widehat{\mathcal{L}}_1(s_1, p) = \arg \max_{\mathcal{L}} P(\mathcal{L}|s_1, p). \quad (22)$$

The depolarizing probability value p and the *a priori* information $p_2^q(\mathcal{L}_2)$ gleaned from the outer soft-input soft-output (SISO) decoder of Fig. 3 are utilized by the inner SISO decoder for calculating the *extrinsic* information $p_2^e(\mathcal{L}_2)$. For the first iteration, the inner SISO decoder only has the depolarizing probability p as the input. Thus, the value of *a priori* information $p_2^q(\mathcal{L}_2)$ is initialized to be equiprobable. Next, an interleaver is utilized to transform the output of the inner SISO decoder, namely the *extrinsic* information $p_2^e(\mathcal{L}_2)$ to *a priori* information $p_1^q(\mathcal{P}_1)$ as the input of the outer SISO decoder. By combining the *a priori* information $p_1^q(\mathcal{P}_1)$ and the syndrome value s_1 , the outer SISO decoder of Fig. 3 calculates the *extrinsic* information $p_1^e(\mathcal{P}_1)$. The *extrinsic* information $p_1^e(\mathcal{P}_1)$ is then deinterleaved to yield the *a priori* information $p_2^q(\mathcal{L}_2)$, which is fed into the inner SISO decoder. This whole process is performed iteratively until one of the following conditions is satisfied: 1) the converged mutual information is attained; 2) the maximum affordable number of iterations l is reached. At the final iteration, the outer SISO decoder produces $\widehat{\mathcal{L}}_1$, which is the most likely error pattern, given the value of p and s_1 provided by the quantum part of Fig. 3. Finally, the recovery operator $\mathcal{R} = \widehat{\mathcal{L}}_1$ is applied to complete the error correction.

IV. EXIT CHART ANALYSIS

A. THE FUNDAMENTALS

In the classical domain, EXIT charts are utilized for visualizing the convergence behaviour of iterative decoding schemes, which is based on the average mutual information (MI) at the input and the output of the constituent decoders. The EXIT chart was originally proposed by ten Brink [23], [24] for dispensing with the exhaustive Monte-Carlo simulations of classical error-correction codes. However, as the research progressed, EXIT charts have also been shown to be a very powerful tool for designing near-capacity error-correction codes without resorting to tedious distance spectrum analysis. Therefore, they have been extensively exploited for designing near-capacity classical [27], [28] as well as quantum error-correction codes [16], [20].

The main differences between the EXIT chart used for classical error correction codes and their quantum counterparts have been extensively discussed in [16] and [20]. In summary, quantum stabilizer codes only infer information about the quantum errors through syndrome measurements, while classical error correction codes allow the measurement of the input bits of the inner encoder (and output bits of the outer encoder). As a result, the main difference of the EXIT chart for quantum error correction codes

is that it models the a-priori information related to the error-sequence corresponding to the input qubits of the inner quantum encoder, instead of the input bits of the inner encoder themselves, which is in contrast to classical codes.

Let us revisit the iterative decoder of our MR-QSBC-QURC depicted in Fig 3. In this scenario, the EXIT chart is utilized for visualizing the exchange of four MI terms, namely the average *a priori* MI I_{A,\mathcal{L}_2} of the inner decoder, the average *a priori* MI I_{A,\mathcal{P}_1} of the outer decoder, the average *extrinsic* MI I_{E,\mathcal{L}_2} of the inner decoder, and finally, the average *extrinsic* MI I_{E,\mathcal{P}_1} of the outer decoder. The input-output relation between I_{A,\mathcal{L}_2} and I_{E,\mathcal{L}_2} constitutes the EXIT curve of the inner decoder, which can be simply referred to as the *inner decoder's EXIT curve*, while that of I_{A,\mathcal{P}_1} and I_{E,\mathcal{P}_1} represents the EXIT curve of the outer decoder, which can be simply referred to as the *outer decoder's EXIT curve*. For a full discourse on how to calculate the MI terms for the inner and outer decoders, we refer the enthusiastic readers to [16] and [20].

A pivotal metric required for understanding EXIT-chart aided QTCs design is the quantum domain counterpart of the classical communication capacity, namely the quantum hashing bound. To elaborate a little further, for a QSC \mathcal{C} having a sufficiently high number of physical qubits exhibiting a quantum coding rate of r_Q , there exists a limit $p^* = p(r_Q)$ below which it can operate yielding an infinitesimally low QBER. Conversely, for a given depolarizing probability p , we can find a QSC \mathcal{C} exhibiting a quantum coding rate of $r_Q \leq C_Q(p)$ and having a sufficiently high number of physical qubits that is capable of yielding an infinitesimally low QBER. This specific limit is referred to as the quantum hashing bound, which is based on the following definition.

Definition 3 (Quantum Hashing Bound [13], [16], [44], [45]): Given a quantum depolarizing channel having a depolarizing probability p , the quantum hashing bound is defined as

$$C_Q(p) = 1 - H(p) - p \log_2 3, \quad (23)$$

where $H(p)$ is the binary entropy of p defined as $H(p) = -p \log_2 p - (1-p) \log_2 (1-p)$. Given a value of p , then $C_Q(p)$ is the quantum hashing bound for p . Conversely, given a value of r_Q , the value of $p^* = p(r_Q)$ represents the quantum hashing bound for r_Q .

Hence, the goal of designing a QSC exhibiting a quantum coding rate r_Q is to ensure that it can operate as close as possible to the limit of $p^* = p(r_Q)$. Similarly, given the depolarizing probability p , we may design a QSC exhibiting r_Q very close to $C_Q(p)$, yielding an infinitesimally low QBER. For instance, a QSC having a quantum coding rate of $r_Q = 1/2$, the quantum hashing bound is given by $p^* = 0.074$. Conversely, for a quantum depolarizing channel having a depolarizing probability $p = 0.050$, the quantum hashing bound is given by $C_Q(p) = 0.634$.

B. INNER EXIT CURVES

The QTC design advocated in this treatise relies on the concatenation of MR-QSBCs as the outer codes and a QURC as the inner code. As the terminology suggested, a QURC is a quantum convolutional code (QCC) having a quantum coding rate of unity ($r_Q = 1$). To conceive a QTC design having a near-capacity error correction performance, it is highly desirable that QCC encoders exhibit recursive and non-catastrophic properties as defined in [15]. The recursive structure of QCCs is required for ensuring the convergence of iterative decoding to a vanishingly low QBER. Meanwhile, the QCCs that exhibit catastrophic structure require a doping mechanism or entanglement-assisted solution in order to substantially benefit from iterative decoding, since catastrophic QCCs provide zero *a priori* information [45], [46]. Unfortunately, the QCCs cannot be simultaneously recursive and non-catastrophic [47].

To circumvent these impediments of constructing a *good* QCC, a non-recursive and non-catastrophic QURC can be very carefully designed for striking this delicate compromise, since it still can benefit from the iteration gains even if the inner EXIT curve terminates at the $(1, y)$ point for $y < 1$, as long as it only intersects with the outer EXIT curve very close to $(x, y) = (1, 1)$ point. Obeying these stringent constraints, an exhaustive EXIT-chart based heuristic search has been conducted to find a *good* non-recursive and non-catastrophic QURC. The resultant memory-2 QURC has the following seed transformation [21]⁴:

$$\mathcal{U} = \{21, 56, 5, 46, 44, 38\}_{10}. \quad (24)$$

For the rest of this treatise the QURC specified in (24) will be employed as our inner code in the MR-QSBC-QURC scheme advocated.

Figure 4(a) portrays the inner EXIT curves of the selected QURC in (24) for depolarizing probability values of $p = \{0.08, 0.07, 0.06, 0.05\}$. We also depict the outer EXIT curve of the half-rate QSBC given in Fig. 1(a). For a half-rate QSC ($r_Q = 1/2$), the quantum hashing bound is given by $p^* = 0.074$ based on (23). Therefore, the p values used for generating the inner EXIT curves are selected around p^* . In Fig. 4(a), we can observe that for $p = 0.07$, the inner and outer EXIT curves intersect very early. As we decrease the depolarizing probability to $p = 0.06$, a marginally open tunnel between the inner and outer EXIT curves can be seen, which means that at this p value the concatenation between half-rate QSBCs and a QURC will start to glean iterative decoding gains. However, we can also see in the inset of Fig. 4(a) that the inner and outer EXIT curves intersect before they reach the $(x, y) = (1, 1)$ point, albeit it is very close. As the depolarizing probability value decreases ($p = 0.05$), the inner EXIT curve shifts higher and the intersection point is getting closer to the $(x, y) = (1, 1)$ point. Consequently,

⁴A quantum encoder \mathcal{V} can be represented using a binary matrix V and seed transformation \mathcal{U} is used for simplifying the representation of binary matrix V . A complete tutorial of transforming a quantum encoder \mathcal{V} to its seed transformation \mathcal{U} can be found in [22].

based on the observation with regard to the inner and outer EXIT curves in Fig 4(a), we may predict the QBER curve obtained by the Monte-Carlo simulations: a waterfall-like QBER curve is expected for the p values close to p^* , ($0.05 \leq p \leq 0.6$) followed by an error floor, as the p value decreases ($p < 0.05$). In fact, this simple concatenation of half-rate QSBCs and a QURC has been demonstrated to provide an excellent error correction performance near the quantum hashing bound in [22], as predicted accurately by the EXIT curves presented in Fig. 4(a).

C. OUTER EXIT CURVES

In contrast to the inner decoder's EXIT curve, the outer decoder's EXIT curve is independent of the depolarizing probability value of the quantum depolarizing channel, since the *a priori* information obtained by the outer code is provided by the inner code, not by the quantum channel. Therefore, the outer EXIT curve of the QSBCs only depends on its quantum coding rate. Based on the quantum encoders of MR-QSBCs illustrated in Fig. 1 and 2, the seed transformations of the MR-QSBCs are given in Table 3. Figure 4(b) portrays the outer EXIT curves of the proposed MR-QSBCs exhibiting the quantum coding rates of $r_Q = \{3/4, 2/3, 1/2, 1/3, 1/4\}$. We can observe from Fig. 4(b) that as the quantum coding rate increases, the outer EXIT curve shifts higher. Consequently, the inner code has to operate at a lower depolarizing probability to appropriately attain a marginally open tunnel between the inner and outer EXIT curves, which is a trend we also learned from Fig. 4(a). Similarly, we can also infer approximately the p values required by the QURC as the inner code based on the quantum hashing bound p^* to produce a marginally open tunnel. Explicitly, given the quantum coding rate of the QSBCs $r_Q = \{3/4, 2/3, 1/2, 1/3, 1/4\}$, we obtain $p^* = \{0.116, 0.094, 0.074, 0.056, 0.039\}$.

We will utilize the results in Fig. 4(b) for optimizing the MR-QSBCs as the outer codes of the proposed MR-QSBC-QURC scheme in the following subsection. Each of the MR-QSBCs having a different quantum coding rate will serve as a subcomponent code. It is important to note that although we only consider five subcomponent codes in this treatise, the range of MR-QSBC quantum coding rates can be readily extended to the higher as well as lower quantum coding rates to increase the number of subcomponent codes by directly following the discussions of Section II.

D. EXIT-CHART AIDED DESIGN

The primary objective of the EXIT-chart aided QTC design is to obtain the best possible inner and outer code combination by evaluating their inner and outer EXIT curves. Assuming we have many copies of the MR-QSBCs encoders, our design objective is to find the optimal configuration of the outer codes constituted by MR-QSBCs, which provides the best match to the given inner code – in this case to the QURC. The optimization is performed by utilizing the EXIT-chart based heuristic search by finding the optimal outer EXIT

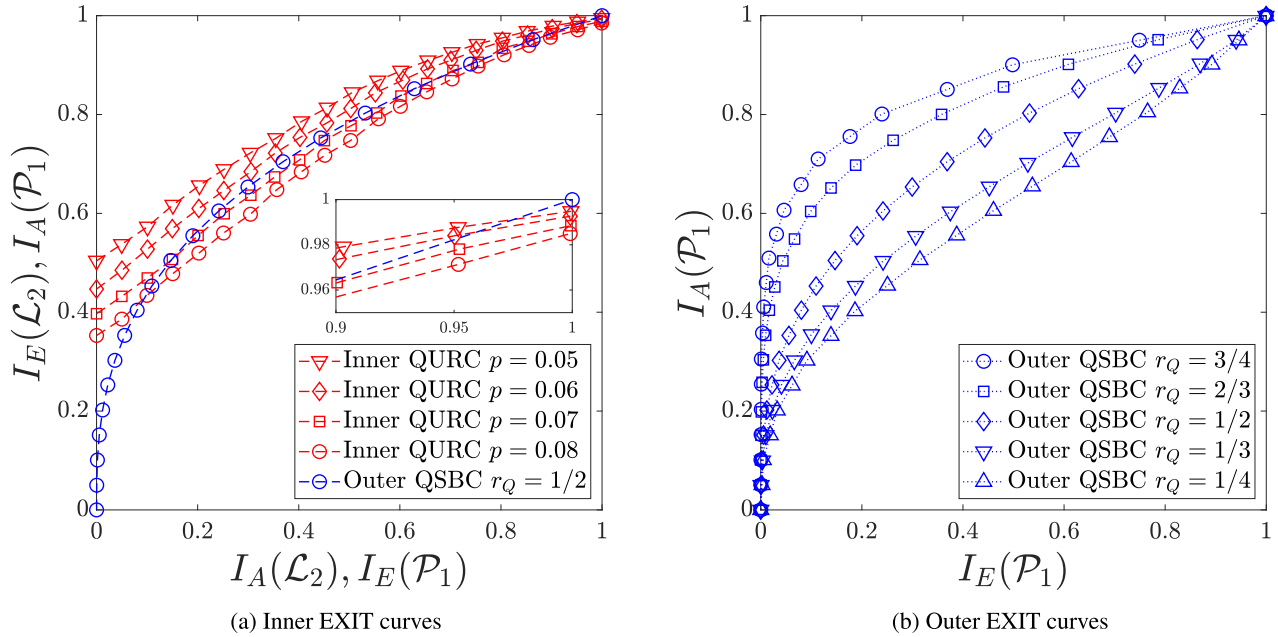


FIGURE 4. (a) The inner EXIT curves for non-recursive and non-catastrophic QURC and the outer EXIT curve of a half-rate QSBC. The quantum hashing bound is $p^* = 0.074$. (b) Outer EXIT curves for MR-QSBCs.

TABLE 3. The seed transformation \mathcal{U} associated with the subcomponent MR-QSBCs exhibiting various quantum coding rates r_q .

r_q	\mathcal{U}
1/4	{34560, 18176, 58368, 53760, 51456, 228, 210, 201, 184, 120, 32, 16, 8, 1024, 512, 256} ₁₀
1/3	{2240, 1216, 3712, 3392, 58, 53, 44, 28, 8, 4, 128, 64} ₁₀
1/2	{144, 80, 240, 15, 10, 6, 2, 16} ₁₀
2/3	{2112, 1088, 576, 320, 4032, 63, 34, 18, 10, 6, 2, 64} ₁₀
3/4	{33024, 16640, 8448, 4352, 2304, 1280, 65280, 255, 130, 66, 34, 18, 10, 6, 2, 256} ₁₀

curve having a marginally open tunnel with regard to the inner EXIT curve at a depolarizing probability close to the quantum hashing bound of the quantum coding rate required. More specifically, due to the inherent flexibility of our proposed MR-QSBCs encoders, we may design a QTC that exploits not only the quantum encoder that exhibits a single quantum coding rate. More precisely, we may configure the MR-QSBCs as the outer codes so that they encode a specifically designed fraction of the K logical qubits. The fraction of the logical qubits is determined by the weighting coefficient satisfying the following constraints [25], [26]:

$$r_Q = \sum_{q=1}^Q r_q w_q, \text{ s.t. } \sum_i w_i = 1, \quad (25)$$

where r_Q is the target of quantum coding rate, Q is the number of subcomponent codes, r_q is the subcomponent quantum coding rate, and w_q is the weighting coefficient of the subcomponent code subjected to the normalization. Since we employ multiple-rate QSBCs as the outer codes of our proposed MR-QSBC-QURC scheme, we have $r_q = \{1/4, 1/3, 1/2, 2/3, 3/4\}$. Therefore, our design objective

can be reformulated as that of finding the weighting coefficient w_q to produce the optimal MR-QSBC-QURC design.

Let us now formally define the inner and outer EXIT curves presented in Subsection IV-B and IV-C. Firstly, the inner EXIT curve can be formally described as a transfer function T_1 mapping the average MI I_{A, \mathcal{L}_2} of the *a priori* information to the average MI I_{E, \mathcal{L}_2} of the *extrinsic* information by taking into account the depolarizing probability p as follows:

$$I_{E, \mathcal{L}_2} = T_1[I_{A, \mathcal{L}_2}, p]. \quad (26)$$

Secondly, similar to the inner EXIT curve, the outer EXIT curve can be formally described as a transfer function T_2 mapping the average MI I_{A, \mathcal{P}_1} of the *a priori* information to the average MI I_{E, \mathcal{P}_1} of the *extrinsic* information as follows:

$$I_{E, \mathcal{P}_1} = T_2[I_{A, \mathcal{P}_1}]. \quad (27)$$

Notice that in Fig. 4(b), we inverted the plot of the outer EXIT curves, since the *extrinsic* information provided by the outer code is utilized as the *a priori* information of the inner code. Therefore, the outer EXIT curves portrayed in Fig. 4(b) are

more accurately described as

$$I_{A, \mathcal{P}_1} = T_2^{-1}[I_E, \mathcal{P}_1]. \quad (28)$$

Let Q be the number of MR-QSBCs subcomponent codes. In this treatise, we have $Q = 5$, and $T_{2,q}^{-1}$ is the outer EXIT curve of the q -th subcomponent code for $q = \{1, \dots, Q\}$. Therefore, the resultant outer EXIT curve I_{E, Q, \mathcal{P}_1} of the MR-QSBCs after fractional encoding using the weighting coefficients of (25) can be determined as

$$I_{E, Q, \mathcal{P}_1} = T_{2, Q}^{-1}[I_A, \mathcal{P}_1] = \sum_{q=1}^Q w_q T_{2, q}^{-1}[I_A, \mathcal{P}_1]. \quad (29)$$

To find the optimal weighting coefficient for the MR-QSBCs subcomponent codes, we have to perform a curve matching optimization by minimizing area represented by the the square of errors between the inner and outer EXIT curves. For simplifying the notation, let $T_1[I_A, \mathcal{L}_2, p] = T_1[j, p]$, $T_{2, Q}^{-1}[I_A, \mathcal{P}_1] = T_2^{-1}[j]$, and $T_{2, q}^{-1}[I_A, \mathcal{P}_1] = T_{2, q}^{-1}[j]$ for $j = \{1, \dots, J\}$, where J is the number of sample points displayed in our inner and outer EXIT curves. Therefore, the error can be directly calculated as

$$e[j] = T_1[j, p] - T_{2, q}^{-1}[j], \quad (30)$$

where we have $p = p^* - \epsilon$, given that ϵ is chosen to be arbitrarily small. Therefore, the corresponding matrix-based representation can be written as

$$\mathbf{e} = \mathbf{a} - \mathbf{B}\mathbf{w}, \quad (31)$$

where we have

$$\mathbf{e} = \begin{pmatrix} e[1] \\ e[2] \\ \vdots \\ e[J] \end{pmatrix}, \quad \mathbf{a} = \begin{pmatrix} T_1[1, p] \\ T_1[2, p] \\ \vdots \\ T_1[J, p] \end{pmatrix}, \quad \mathbf{w} = \begin{pmatrix} w_1 \\ w_2 \\ \vdots \\ w_Q \end{pmatrix}, \quad (32)$$

$$\mathbf{B} = \begin{pmatrix} T_{2,1}^{-1}[1] & T_{2,2}^{-1}[1] & \cdots & T_{2,Q}^{-1}[1] \\ T_{2,1}^{-1}[2] & T_{2,2}^{-1}[2] & \cdots & T_{2,Q}^{-1}[2] \\ \vdots & \vdots & \ddots & \vdots \\ T_{2,1}^{-1}[J] & T_{2,2}^{-1}[J] & \cdots & T_{2,Q}^{-1}[J] \end{pmatrix}.$$

Since we do not want the inner and outer EXIT curves to cross-over far from the (1, 1) point, we have to impose an additional constraint that guarantees a marginally open tunnel between the inner and outer EXIT curves, which can be explicitly expressed as

$$e[j] > 0 \text{ for } j = \{1, \dots, J\}. \quad (33)$$

Thus, the cost function used for finding the weighting coefficients \mathbf{w} is given by

$$E(\mathbf{w}) = \sum_{j=1}^J e[j]^2 = \mathbf{e}^T \mathbf{e}. \quad (34)$$

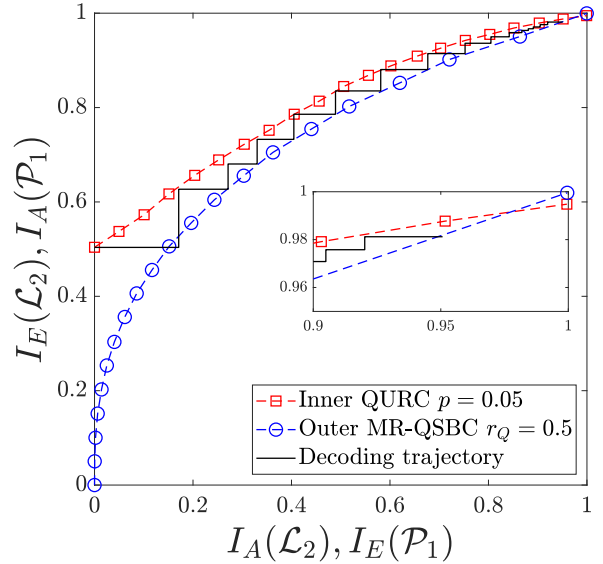


FIGURE 5. Decoding trajectory of MR-QSBC-QURC at the depolarizing probability of $p = 0.05$. The inner code is a non-recursive and non-catastrophic QURC and the outer code is the optimized MR-QSBCs having $r_Q = 0.5$. The quantum hashing bound is $p^* = 0.074$.

Finally, the overall EXIT-chart based curve matching required for finding the optimal weighting coefficient $\hat{\mathbf{w}}$ can be summarized as

$$\hat{\mathbf{w}} = \arg \min_{\mathbf{w}} E(\mathbf{w}), \quad (35)$$

which is subject to (25) and (33). The unconstrained optimization of (35) can be iteratively solved using the gradient descent method, where we have

$$\frac{\partial E(\mathbf{w})}{\partial \mathbf{w}} = 2\mathbf{e}. \quad (36)$$

The solutions are then reevaluated according to the constraints (25) and (33). For a full discourse on the EXIT-chart based optimization algorithm of finding the optimal weighting coefficient $\hat{\mathbf{w}}$, we refer the enthusiastic readers to [25] and [26].

We now present the results of the aforementioned optimization algorithm after optimizing the MR-QSBCs as the outer codes for the proposed MR-QSBC-QURC. Figure 5 depicts the iterative decoding trajectory of our MR-QSBC-QURC, where the inner code is constituted by the QURC of (24) and the outer code is constituted by the optimized MR-QSBCs having $r_Q = 0.5$. Explicitly, by implementing the optimization algorithm we just described, we found that the optimal weighting coefficient $\hat{\mathbf{w}}$ of half-rate MR-QSBCs matching the inner EXIT curve of the QURC at $p = 0.05$ is given by $\hat{\mathbf{w}} = \{0, 0.60, 0, 0, 0, 40\}$. It can be immediately verified that the constraints in (25) and (33) are satisfied. The decoding trajectory represents the iterative MI improvements based on the information exchange between the inner and outer decoders, which is illustrated by the stair-case-like curve in Fig. 5. We can observe a marginally open tunnel

between the inner and outer EXIT curves that guarantees the convergence of the iterative decoding to vanishingly low QBER. In the inset of Fig. 5, the decoding trajectory terminates before reaching the $(x, y) = (1, 1)$ point due to the non-recursive and non-catastrophic nature of the QURC encoder. Therefore, we expect to witness an error-floor in its QBER curve.

To demonstrate that the proposed MR-QSBC-QURC scheme can be designed to cater for a wide range of quantum coding rate requirements, we have also performed EXIT-chart aided optimization for our MR-QSBCs covering quantum coding rates of $r_Q = \{0.3, 0.4, 0.6, 0.7\}$ and the results are presented in Fig. 6. Similarly, each of the MR-QSBCs have been optimized to match the inner EXIT curve at a depolarizing probability p close to their respective quantum hashing bounds p^* . The resultant optimal weighting coefficient \hat{w} obtained for all the target quantum coding rates evaluated are summarized in Table 4. We can observe in Fig. 6 that all the inner and outer EXIT curves of the MR-QSBC-QURC designed provide a marginally open tunnel for the p values close to the quantum hashing bound p^* and the decoding trajectories terminate really close to the $(x, y) = (1, 1)$ point. We note that the decoding trajectory terminates earlier for MR-QSBCs exhibiting lower r_Q . Consequently, we predict that the QBER curve of MR-QSBC-QURC having $r_Q = 0.3$ will have a higher error floor than the MR-QSBC-QURC having $r_Q = 0.7$. We have to reiterate once again that the proposed MR-QSBC-QURC scheme may be designed and be optimized for arbitrary values of $0 < r_Q < 1$.

V. MULTIPLE-RATE QUANTUM TURBO SHORT-BLOCK CODES

This section is dedicated to validating our EXIT-chart aided design presented in Section IV. We evaluate the performance of the proposed MR-QSBC-QURC scheme in terms of its QBER, their distance to the quantum hashing bound, and finally, the achievable goodput through Monte-Carlo simulations. For this purpose, we consider the MR-QSBC-QURC having the target quantum coding rates of $r_Q = \{0.3, 0.4, 0.5, 0.6, 0.7\}$, with their quantum hashing bounds given by $p^* = \{0.116, 0.094, 0.074, 0.056, 0.039\}$. To produce simulation results having significant appeal for near-future implementation, we consider a moderate number of logical qubits, namely $K = \{500, 1000, 2000\}$ for all the schemes considered during the simulations.

A. QBER

In this treatise, we define the qubit error ratio (QBER) as the ratio between the number errors imposed on the logical qubits $|\widehat{\psi}_1\rangle^{K_1}$ after applying the recovery \mathcal{R} at the end of the decoding of MR-QSBC-QURC to the total number of logical qubits simulated. First, we compare the QBER of the proposed half-rate MR-QSBC-QURC scheme to that of half-rate QTCs using QIRCCs as the outer codes and a QURC as the inner code, which we refer to as QIRCC-QURC. Similar

TABLE 4. The result of subcomponent codes optimal weighting coefficient \hat{w}_i obtained from EXIT-chart based exhaustive curve matching for various target of quantum coding rates r_Q . The subcomponent quantum coding rates are $r_q = \{1/4, 1/3, 1/2, 2/3, 3/4\}$.

r_Q	\hat{w}_i
0.3	{0.44 0.54 0.02 0 0}
0.4	{0.11 0.44 0.46 0 0}
0.5	{0 0.60 0 0 0.40}
0.6	{0 0 0.60 0 0.40}
0.7	{0 0 0.20 0 0.80}

to our proposed scheme, the outer code of QIRCC-QURC is also optimized using the EXIT-chart based heuristic search presented in Section IV. The main difference is that the outer codes of the QIRCC-QURC are composed by QCC subcomponent codes. More specifically, the seed transformation \mathcal{U} of the QCC subcomponent codes utilized as the outer codes is described in Table 5. The EXIT-chart based optimal weighting coefficients of half-rate QIRCC-QURC scheme are given by $\hat{w} = \{0.1316, 0.1869, 0.2962, 0.3852, 0\}$. The outer codes of QIRCC-QURC exhibit a stronger error-correction capability than the outer codes of MR-QSBC-QURC, which are constituted by MR-QSBC that exhibit a minimum distance of $d = 2$. Additionally, the QIRCC-QURC also represents the best-performing half-rate QCC-based QTC in the open literature. However, as we have elaborated on earlier, our proposed MR-QSBC-QURC scheme has the advantage that it can be designed to accommodate arbitrary quantum coding rates using only a single quantum encoder. By contrast, puncturing QCCs may result in QCCs that do not satisfy the symplectic criterion.

Figure 7 depicts the QBER comparison between the half-rate MR-QSBC-QURC and half-rate QIRCC-QURC schemes. The quantum hashing bound of half-rate QSCs is given by $p^* = 0.074$, marked by the red dashed line. The maximal number of iterations invoked for both schemes is $l = 16$. The QBER curves of the QIRCC-QURC scheme are represented by the black dashed lines, while those of the MR-QSBC-QURC scheme are depicted using blue solid lines.

We observe from Fig. 7 that both schemes provide QBER improvements as the number of physical qubits increases, which is the expected trend based on the pertinent quantum coding trade-offs [31]. Furthermore, as we have predicted using the EXIT chart analysis of Section IV, that the QBER waterfall region of MR-QSBC-QURC can be seen in the region of $0.04 < p < 0.06$. However, as the depolarizing probability decreases, an error floor emerges, which is expected, since we have witnessed in our EXIT chart analysis that the decoding trajectory terminates before reaching the $(x, y) = (1, 1)$ point due to the crossover between the inner and outer EXIT curves. Having said that, the waterfall region of the QBER curve appears near to the quantum hashing bound.

Compared to the QIRCC-QURC, the QBER curve of the MR-QSBC-QURC intersects with the uncoded QBER curve

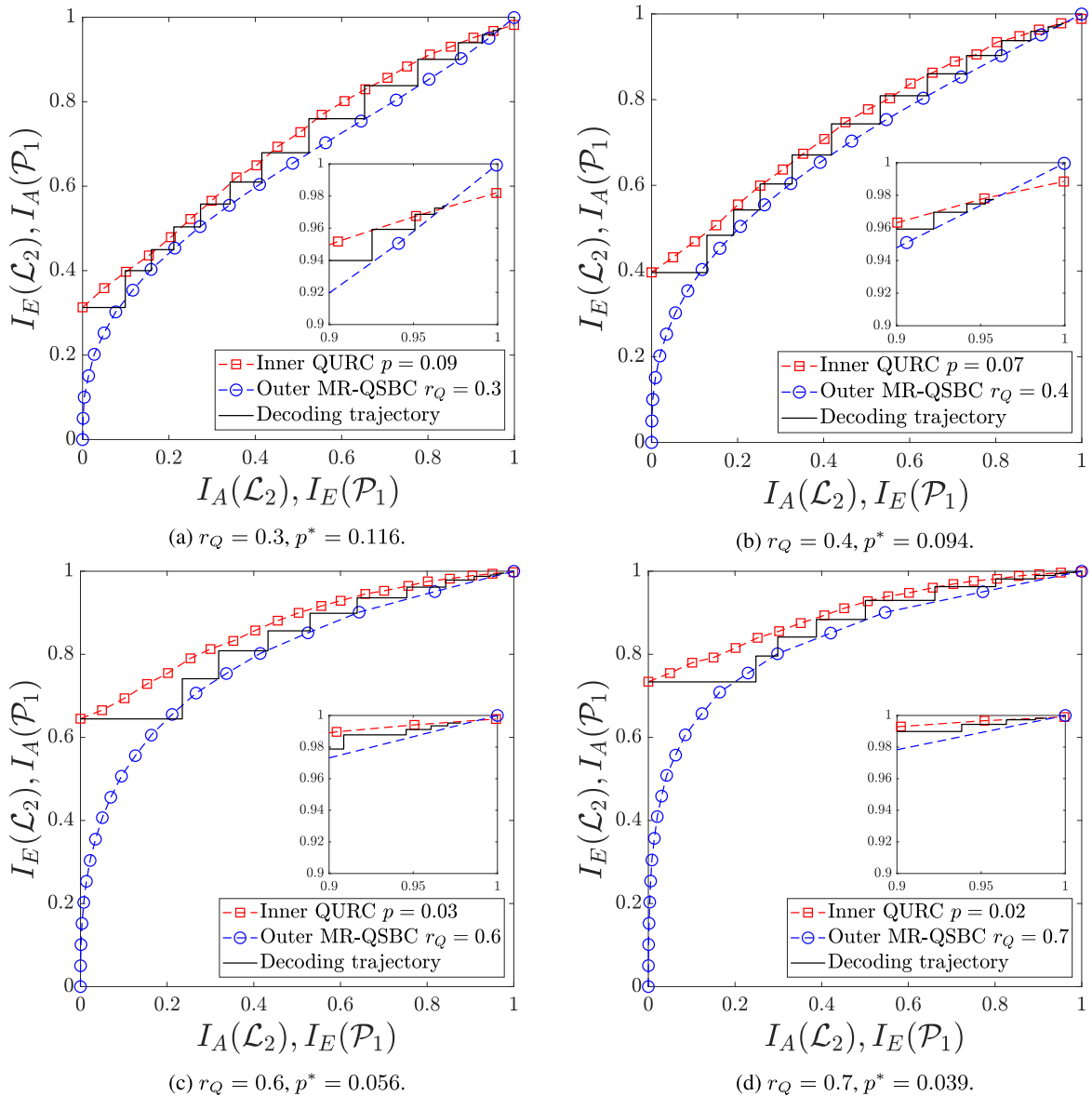


FIGURE 6. The decoding trajectories of MR-QSBC-QURC exhibiting various quantum coding rates.

TABLE 5. The seed transformation \mathcal{U} associated with QCC subcomponent codes exhibiting various quantum coding rates r_q for constructing the QrCC-QURC of [21]. All of the QCCs exhibiting a memory of $m = 3$.

r_q	\mathcal{U}
1/4	{9600, 691, 11713, 4863, 1013, 6907, 1125, 828, 10372, 6337, 5590, 11024, 12339, 3439} ₁₀
1/3	{3968, 1463, 2596, 3451, 1134, 3474, 657, 686, 3113, 1866, 2608, 2570} ₁₀
1/2	{848, 1000, 930, 278, 611, 263, 744, 260, 356, 880} ₁₀
2/3	{529, 807, 253, 1950, 3979, 2794, 956, 1892, 3359, 2127, 3812, 1580} ₁₀
3/4	{62, 6173, 4409, 12688, 7654, 10804, 1763, 15590, 6304, 3120, 2349, 1470, 9063, 4020} ₁₀

at a higher depolarizing probability value in Fig. 7. For instance, let us observe the scenario of $K = 2000$. In Fig. 7, we locate the cross-over point between the uncoded QBER curve and the QBER curve of the MR-QSBC-QURC at $p = 0.058$. Meanwhile, the QBER curve of the QrCC-QURCC

intersects at $p = 0.043$. Thus, the proposed scheme provides a higher coding gain when we consider a scenario having the requirement of $\text{QBER} \leq \text{uncoded QBER}$.

Let us now consider in Fig. 3 a case where the requirement is $\text{QBER} \leq 10^{-3}$. We obtain the maximum tolerable

TABLE 6. Performance comparison of half-rate QIrCC-QURC to half-rate MR-QSBC-QURC for logical qubits of $k = \{500, 1000, 2000\}$. The performance is described using the maximum tolerable depolarizing probability p given various requirements, below which the code improves the QBER. The quantum hashing bound is $p^* = 0.074$.

Requirement	$k = 500$		$k = 1000$		$k = 2000$	
	p QIrCC	p QSBC	p QIrCC	p QSBC	p QIrCC	p QSBC
QBER \leq Uncoded	0.037	0.054	0.039	0.057	0.043	0.058
QBER $\leq 10^{-3}$	0.028	0.034	0.033	0.040	0.037	0.044
QBER $\leq 10^{-4}$	0.024	0.015	0.029	0.022	0.035	0.027

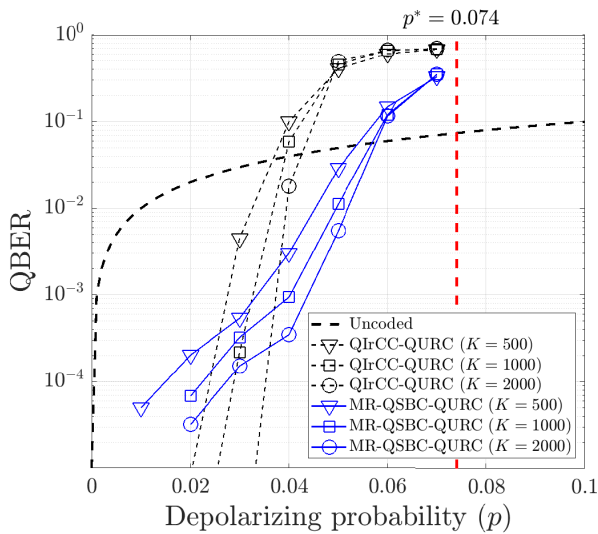


FIGURE 7. The QBER comparison between half-rate QIrCC-QURC and MR-QSBC-QURC.

depolarizing probability of $p = 0.044$, below which the MR-QSBC-QURC satisfies the QBER requirement, while for the QIrCC-QURC, we find the maximum tolerable depolarizing probability of $p = 0.037$. In this scenario, the MR-QSBC-QURC advocated still outperforms the QIrCC-QURC. However, when we consider the case where the requirement is $\text{QBER} \leq 10^{-4}$, we find that the depolarizing probability threshold must be lower for MR-QSBC-QURC than for QIrCC-QURC to avoid the emergence of an error floor. More specifically, for the MR-QSBC-QURC, we have $p = 0.027$, while for QIrCC-QURC, we have $p = 0.035$ in Fig. 3. Since the outer code of the QIrCC-QURC is based on an ensemble of QCC subcomponent codes having stronger error correction capabilities than the MR-QSBCs, the QIrCC-QURC tends to further degrade the QBER by imposing additional errors when it tries to perform error correction beyond its capability, instead of correcting them. However, once the QIrCC-QURC operates within its convergence region, it starts correcting more errors than the MR-QSBC-QURC. Therefore, the QBER curve of the QIrCC-QURC intersects with the uncoded QBER at a slightly higher QBER value than the MR-QSBC-QURC, but the former has a steeper QBER curve and lower error floor. Thus, our advocated scheme performs well at relatively high quantum depolarizing probabilities, providing reasonably

TABLE 7. The maximum tolerable depolarizing probability p given various QBER requirements and different numbers of logical qubits K , below which the code improves the QBER of MR-QSBC-QURC.

Requirement	QBER \leq Uncoded				
	$r_Q = 0.3$	$r_Q = 0.4$	$r_Q = 0.5$	$r_Q = 0.6$	$r_Q = 0.7$
$K = 500$	0.089	0.073	0.054	0.036	0.021
$K = 1000$	0.091	0.075	0.057	0.039	0.024
$K = 2000$	0.094	0.077	0.058	0.040	0.025
Requirement	QBER $\leq 10^{-3}$				
	$r_Q = 0.3$	$r_Q = 0.4$	$r_Q = 0.5$	$r_Q = 0.6$	$r_Q = 0.7$
$K = 500$	0.069	0.055	0.034	0.023	0.012
$K = 1000$	0.070	0.061	0.040	0.029	0.017
$K = 2000$	0.074	0.065	0.044	0.032	0.022

low QBER. However, once the MR-QSBC-QURC operates at lower depolarizing probabilities within its convergence region, we may switch the MR-QSBC-QURC to a higher quantum coding rate for meeting the QBER requirement. The summary of our QBER comparisons between QIrCC-QURC and MR-QSBC-QURC is provided in Table 6.

To provide a complete picture of the MR-QSBC-QURC performance, Fig. 8 portrays the QBER of the MR-QSBC-QURC having various quantum coding rates. Recall that all the outer codes of MR-QSBC-QURC can be represented by a single quantum encoder, along with the optimal weighting coefficient \hat{w} required for performing fractional encoding. In Fig. 8, we indicate the quantum hashing bound for each quantum coding rate with red dashed line. Since the outer codes have been specifically designed using EXIT-chart based optimization, as expected, the waterfall region of their QBER curves appears near to their respective quantum hashing bound p^* . Additionally, the error floor of the MR-QSBC-QURC having a higher quantum coding rate is lower than that of their counterparts having lower quantum coding rate, since during the EXIT chart analysis the inner and outer EXIT curves of the higher quantum coding rate intersects closer to the $(x, y) = (1, 1)$ point. However, for a high quantum coding rate, the error floor is low enough to become invisible, since it would require excessive time to capture the qubit errors by simulations involving limited numbers of physical qubits. We summarize the maximum tolerable depolarizing probability for meeting the requirement of $\text{QBER} \leq$ uncoded QBER as well as $\text{QBER} \leq 10^{-3}$ in Table 7.

It is worth emphasizing that the cost of achieving a lower QBER is an increase in the depth of the quantum encoder

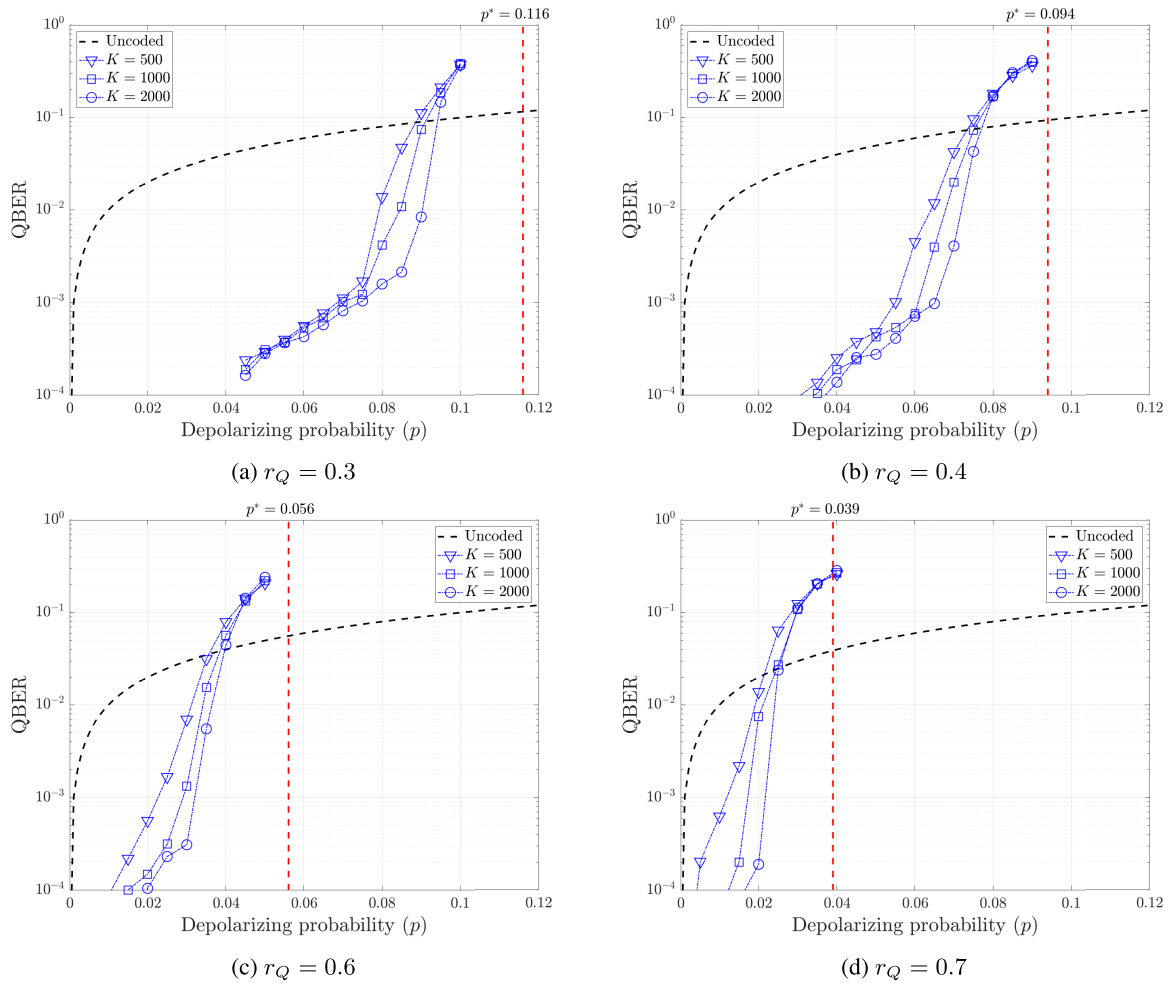


FIGURE 8. The QBER performance of MR-QSBC-QURC exhibiting various quantum coding rates r_Q . The red dashed line represents the quantum hashing bound of the associated quantum coding rate r_Q .

and quantum inverse encoder, as well as an increase in the complexity of the classical decoder. Explicitly, the QBER performance of MR-QSBC-QURC exhibiting different quantum coding rates was evaluated while keeping both the number of logical qubits (K) and the number of decoding iterations fixed ($l = 16$). Therefore, the main factor affecting the encoding and decoding complexity of the MR-QSBC-QURC is the number of physical qubits. More specifically, for QSBCs used as outer codes, the depth of the quantum encoder is independent of the number of physical qubits (N). By contrast, for the QURC used as inner code - which belongs to the family of quantum convolutional codes - the depth of the quantum encoder is linearly proportional to the number of auxiliary qubits ($N - K$). Since the quantum inverse encoder is the reversed version of the quantum encoder, its depth is also identical to that of the quantum encoder. On the other hand, the complexity of the classical decoder is linearly proportional to the length of the classical syndrome vector constituted by the $(N - K)$ classical bits inferred from the measurements of the erroneous auxiliary qubits. For example,

for a quantum coding rate of $r_Q = 1/2$ and $K = 1000$ logical qubits the length of the syndrome vector is $(N - K) = 1000$ bits. By comparison, for an MR-QSBC-QURC having the same quantum coding rate of $r_Q = 1/2$, but encoding $K = 2000$ logical qubits, the length of the syndrome vector is $(N - K) = 2000$ bits. Similarly, when fixing the number of logical qubits to $K = 1000$, but reducing the quantum coding rate to $r_Q = 1/4$, the length of the syndrome vector becomes $(N - K) = 3000$ bits. In both examples, we observe that a QBER performance improvement is attained by increasing the complexity of the classical decoder.

B. DISTANCE FROM THE QUANTUM HASHING BOUND

It is clear from the results presented in Fig. 8 that by reducing the quantum coding rate of MR-QSBC-QURC, we are capable of correcting the errors imposed by the quantum depolarizing channels having higher depolarizing probability. We summarize the results of Fig. 8 in Fig. 9(a) by considering the QBER results for $K = 2000$. Indeed, the results follow

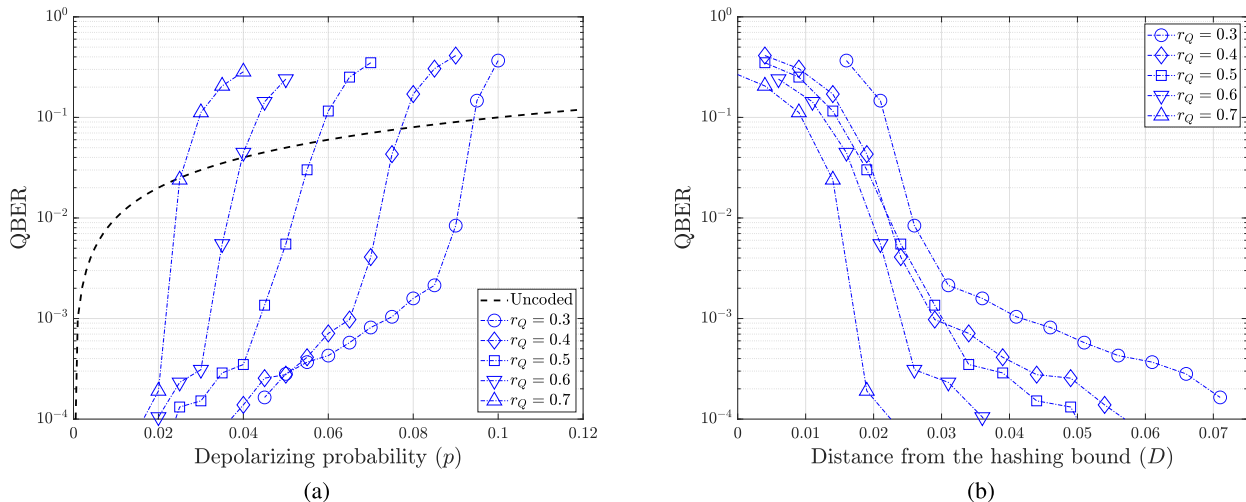


FIGURE 9. The QBER of the MR-QSBC-QURCs exhibiting various quantum coding rates $r_Q = \{0.3, 0.4, 0.5, 0.6, 0.7\}$ versus: (a) depolarizing probability p ; (b) the distances to the quantum hashing bound D . The MR-QSBC-QURCs are used for protecting $K = 2000$ logical qubits.

the expected trends – the lower the quantum coding rate, the higher its tolerable depolarizing probability. However, in contrast to classical communication systems, we do not have a quantitative metric that directly takes into account the quantum coding rate differences of the QSCs having different quantum coding rates. Since the QBER is plotted versus the depolarizing probability rather than the classical energy per bit to noise power spectral density ratio (E_b/N_0), having an appropriate normalization metric may be beneficial for a fair comparison. Explicitly, it is essential to provide such a normalization, since the most intuitive step to be taken for improving the QBER of any QSC is to reduce their quantum coding rate, which results in encoding fewer logical qubits and/or incorporating more auxiliary qubits. While indeed this improves the QBER, as demonstrated in Fig. 8, it reduces the effective throughput. Therefore, in this treatise, we introduce a pair of additional metrics for transforming the QBER of Fig. 8 by accounting for the different quantum coding rates r_Q , namely, the distance from the quantum hashing bound and the goodput.

Definition 4 (Distance From the Quantum Hashing Bound [22], [34]): Given a quantum coding rate r_Q , p^* represents the quantum hashing bound for r_Q . Therefore, the distance D from the quantum hashing bound is defined by

$$D = p - p^*, \tag{37}$$

where p is the depolarizing probability.

Figure 9(b) explicitly portrays the appropriately shifted version of the QBER curves in Fig. 9(a) according to each of the quantum hashing bounds p^* . More precisely, the quantum hashing bound of QSCs having $r_Q = \{0.3, 0.4, 0.5, 0.6, 0.7\}$ is given by $p^* = \{0.116, 0.094, 0.074, 0.056, 0.039\}$. If we consider $\text{QBER} = 10^{-3}$, we attain the distances of $D = \{0.042, 0.029, 0.030, 0.024, 0.017\}$ from the quantum hashing bound. It is important to highlight that

these near-hashing-bound results are achieved for protecting $K = 2000$ logical qubits using practical non-zero quantum coding rates.

A closer inspection of Fig. 8 reveals that as we reduce the quantum coding rate r_Q , the QBER curve shifts further away from the quantum hashing bound. However, we also have to point out that at higher quantum coding rates, for instance at $r_Q = 0.7$, the quantum hashing bound is as low as at $p^* = 0.039$, which only results in a modest shift of QBER curve. Consequently, the aforementioned absolute distance D from the quantum hashing bound may still require further normalization by the quantum hashing bound p^* for defining the normalized distance from it.

Definition 5 (Normalized Distance From the Hashing Bound): Given a quantum coding rate r_Q , p^* represents the quantum hashing bound and D is the absolute distance from the quantum hashing bound. The normalized distance R from the quantum hashing bound is then defined by

$$R = \frac{D}{p^*}. \tag{38}$$

Using (38), we obtain the normalized distance from the quantum hashing bound for the proposed MR-QSBC-QURC scheme having $r_Q = \{0.3, 0.4, 0.5, 0.6, 0.7\}$ as follows: $R = \{0.362, 0.309, 0.405, 0.429, 0.436\}$. Now, we observe that the higher quantum coding rates exhibit a slightly larger normalized distance from the quantum hashing bound. Since we have individually optimized the MR-QSBC-QURC for different quantum coding rates, the resultant normalized distances from the quantum hashing bound do not exhibit large variations. We argue that the absolute and the normalized distances from the quantum hashing bound provide a balanced view when it comes to comparing the QBER of QSCs having different quantum coding rates.

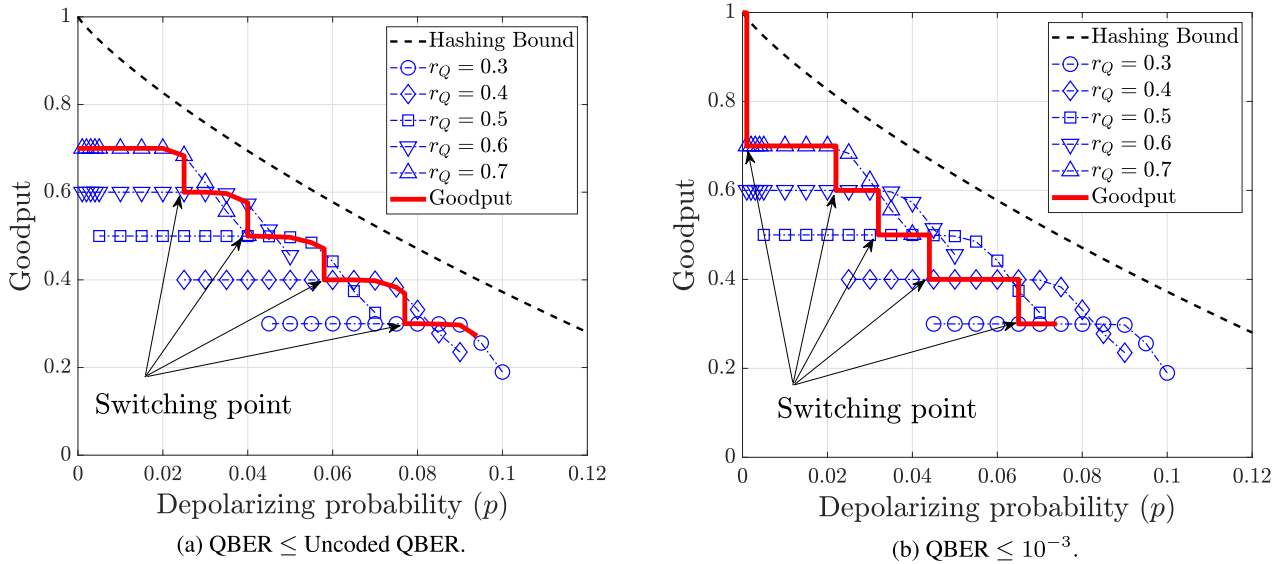


FIGURE 10. The achievable goodput for different QBER requirements: (a) $\text{QBER} \leq \text{Uncoded QBER}$; (b) $\text{QBER} \leq 10^{-3}$. The number of logical qubits $K = 2000$. The switching points are based on the results summarized in Table 7.

C. GOODPUT

The final metric that we consider for comparing the QBER results of Fig. 8 is goodput, which is based on the following definition.

Definition 6 (Goodput [22]): Goodput represents the effective number of logical qubits obtained after error correction, which is defined as the fraction of error-free logical qubits normalized by the quantum coding rate r_Q formulated as follows:

$$G = r_Q(1 - \text{QBER}). \tag{39}$$

We portray the goodput of MR-QSBC-QURC in Fig. 10 for two different QBER requirements. Explicitly, in Fig. 10(a), we show the achievable goodput for $\text{QBER} \leq \text{uncoded QBER}$, while in Fig. 10(b), for $\text{QBER} \leq 10^{-3}$. The MR-QSBC-QURC scheme may commence its operation at a lower quantum coding rate for coping with a high depolarizing probability, but once the QBER requirement is met it may switch to higher quantum coding rates for increasing the goodput. For instance, let us observe Fig. 10(a), where the requirement is $\text{QBER} \leq \text{uncoded QBER}$. Assume that we initially operate at $p = 0.06$, implying that the MR-QSBC-QURC runs at $r_Q = 0.4$. As the quality of the quantum channel improves, the depolarizing probability may reduce to $p = 0.05$. Hence, the MR-QSBC-QURC switches its quantum coding rate to $r_Q = 0.5$, since we can still satisfy the QBER requirement, while yielding a higher goodput. Similarly, consider Fig. 10(b), where the requirement is $\text{QBER} \leq 10^{-3}$. The MR-QSBC-QURC may start operating at $r_Q = 0.4$ when $p = 0.05$. Then, it may switch to $r_Q = 0.5$ once the quantum channel improves to $p = 0.04$ for meeting the QBER requirement, while increasing the goodput. These switching points indicated in Fig. 10 are based on the results summarized in Table 7.

In Fig. 10, we also include the quantum hashing bound as our benchmark. This is because goodput and quantum hashing bound are intimately linked. Explicitly, quantum hashing bound may be viewed as the maximum achievable goodput, when the mandatory requirement is $\text{QBER} = 0$. Let us now imagine that we have infinitely many quantum coding rates to cover all the quantum coding rates of $0 < r_Q < 1$, which is actually plausible for our MR-QSBC-QURC. In that case, the resultant goodput curve will be a perfectly smooth line near-parallel to the quantum hashing bound. Finally, the distance of goodput curve from the quantum hashing bound depends on the codeword length, the higher it is the lower its distance from the quantum hashing bound. Therefore, we suggest that this characteristic curve should be used more prevalently as a fair metric of rate-compatible QSC designs in the future.

Remark 4: The future development of rate-compatible QSCs should aim for achieving the highest goodput possible given the specific QBER requirement and codeword length. Additionally, for attaining a lower low QBER, the achievable goodput is expected to be close from the quantum hashing bound.

D. COMPARISON WITH STATE-OF-THE-ART

Most of the quantum stabilizer codes found in the literature suffer from low quantum coding rates. Moreover, it has proven to be challenging to find a family of quantum stabilizer codes that offers the same level of flexibility as our proposed MR-QSBC-QURC. Recent advancements in the field have introduced two novel QLDPC codes that exhibit relatively high quantum coding rates: multiple-rate (MR) QLDPC codes [48] and spatially-coupled QLDPC codes [49].

In [48], a family of QLDPC codes is proposed, which utilizes a single stabilizer measurement circuit across a wide

range of quantum coding rates. This is in contrast to our proposed MR-QSBC-QURC scheme, which employs a single encoder and inverse decoder circuit. The multiple-rate nature of the proposed QLDPC codes is achieved by utilizing row-circulant matrices within the parity-check matrix. Some of the resulting QLDPC codes achieve quantum coding rates of $r_Q \approx 0.75$ and $r_Q \approx 0.87$, with a convergence region $p \approx 0.0185$ and $p \approx 0.0128$, respectively. The smallest reported number of logical qubits in [48] is $K \approx 2200$. In comparison, our MR-QSBC-QURC scheme with a quantum coding rate of $r_Q = 0.7$ and $K = 2000$ achieves a convergence region of $p = 0.0250$.

Inspired by the powerful classical spatially-coupled (SC) LDPC codes, the quantum version of SC-LDPC codes, known as spatially-coupled QLDPC codes are proposed in [49]. This novel QLDPC codes family demonstrates an impressive error-correction performance, achieving a convergence region around $p = 0.065$ for a quantum coding rate of $r_Q \approx 0.34$ with $K = 2500$ logical qubits and a convergence region around $p = 0.080$ for a quantum coding rate of $r_Q \approx 0.28$ with $K = 1600$ logical qubits. This remarkable performance is largely attributed to an effective algorithm that eliminates all four-cycle and six-cycle configurations in the parity-check matrix. As a comparison, our MR-QSBC-QURC scheme achieves a convergence region of $p = 0.094$ for a quantum coding rate of $r_Q = 0.3$ with $K = 2000$ logical qubits.

E. PRACTICAL ASPECTS

We can see that the MR-QSBC-QURC has immediate potential for applications in quantum-secure direct classical [50], [51] and quantum communications [52]. As quantum communication channels exhibit time-varying characteristics, it becomes essential to have a set of quantum error-correction codes that can efficiently adapt to this dynamic nature. To achieve this, an accurate estimation of the quantum depolarizing channels is crucial in assigning the appropriate quantum coding rate based on the channel quality. One approach for assessing the quality of quantum communication channels involves using known pilot qubits or pre-shared entanglement to estimate the depolarizing probability. However, this method assumes that the quantum depolarizing channel remains static or quasi-static, implying that the depolarizing probability does not vary significantly over time. An alternative approach is to employ syndrome-based depolarizing probability estimation, which draws on classical principles [42], [43].

The potential application of MR-QSBC-QURC in the field of quantum computation is highly intriguing. One notable advantage of multiple-rate quantum turbo codes, compared to other quantum stabilizer codes, is their ability to offer flexible quantum coding rates and accommodate varying numbers of logical qubits, all while ensuring a guaranteed convergence region. However, more research is needed to investigate the feasibility and implementation of error-corrected quantum gates using quantum turbo codes.

VI. CONCLUSION

We have conceived near-hashing-bound single-encoder-based multiple-rate MR-QSBC-QURC using EXIT-chart based heuristic search. The main advantage of our proposed design is that it can be tailored for any arbitrary quantum coding rate r_Q , which is achieved by performing fractional encoding of the MR-QSBCs as the outer codes. This is plausible in the light of our experience with classical error-correction codes design. Despite the low-complexity outer codes, our Monte-Carlo simulation results show that the MR-QSBC-QURC advocated performs near to the quantum hashing bound at $\text{QBER} = 10^{-3}$ for the specific quantum coding rates considered. More precisely, our MR-QSBC-QURC is capable of operating at the distance of $D = \{0.042, 0.029, 0.030, 0.024, 0.017\}$ from the quantum hashing bound for quantum coding rates of $r_Q = \{0.3, 0.4, 0.5, 0.6, 0.7\}$. Despite its low-complexity code constructions, the advocated MR-QSBC-QURC scheme advocated offers a competitive QBER performance even against the best-performing QCC-based QTC in the literature. We believe our solutions will open the pathway for the future development of rate-compatible QSCs capable of adapting to diverse QBER requirements and quantum channel qualities without relying on different quantum encoders.

A. DESIGN GUIDELINES

Based on the discussions throughout this treatise, we provide the following design guidelines for MR-QSBC-QURC capable of operating at various quantum coding rates in line with different quantum channel qualities.

- Determine the MR-QSBC-QURC parameters based on the uncoded QBER, including the expected quantum coding rates r_Q for the given depolarizing probabilities p or vice versa, using the quantum hashing bound of (23).
- Determine the number of MR-QSBC subcomponent codes according to the desired r_Q . In this treatise, we consider only five MR-QSBC subcomponent codes. However, the number of subcomponent codes can be readily extended to both higher and lower quantum coding rates by following Section II.
- For each quantum coding rate, optimize the outer code constituted by MR-QSBCs by choosing the optimal weighting coefficient using the EXIT-chart based heuristic search. The optimization objective is to obtain a marginally open tunnel at the associated depolarizing probability value p between the inner and the outer decoder's EXIT curves, as described in Section IV.
- Perform Monte-Carlo simulations for each MR-QSBC-QURC having different quantum coding rate to determine the switching points for meeting the QBER requirements. These switching points may be utilized for quantifying the achievable goodput of the MR-QSBC-QURC scheme according to the specific QBER requirements, as exemplified in Section V.

B. FUTURE RESEARCH

The development of quantum error-correction codes that possess a small number of physical qubits, high quantum coding rates, and demonstrate robust error correction performance has posed a significant challenge in the field of quantum information. However, recent progress in the field has brought forth notable advancements, particularly in the area of decoding techniques adapted from classical noise-guessing decoding for the quantum domain [53], [54]. One such approach, known as quantum-aided GRAND, has emerged as a versatile and promising method that exhibits universality across various quantum stabilizer decoding paradigms. This innovative decoding technique has demonstrated exceptional error-correction performance, particularly for quantum stabilizer codes with a modest number of physical qubits. Given these exciting developments, it becomes highly intriguing to explore the potential of applying the quantum-aided GRAND approach to decode MR-QSBC-QURC codes.

REFERENCES

- [1] P. W. Shor, "Scheme for reducing decoherence in quantum computer memory," *Phys. Rev. A, Gen. Phys.*, vol. 52, no. 4, pp. R2493–R2496, Oct. 1995.
- [2] A. M. Steane, "Error correcting codes in quantum theory," *Phys. Rev. Lett.*, vol. 77, no. 5, p. 793, 1996.
- [3] Z. Babar, D. Chandra, H. V. Nguyen, P. Botsinis, D. Alanis, S. X. Ng, and L. Hanzo, "Duality of quantum and classical error correction codes: Design principles and examples," *IEEE Commun. Surveys Tuts.*, vol. 21, no. 1, pp. 970–1010, 1st Quart., 2019.
- [4] G. Cariolaro and G. Pierobon, "Performance of quantum data transmission systems in the presence of thermal noise," *IEEE Trans. Commun.*, vol. 58, no. 2, pp. 623–630, Feb. 2010.
- [5] A. S. Cacciapuoti, M. Caleffi, R. Van Meter, and L. Hanzo, "When entanglement meets classical communications: Quantum teleportation for the quantum internet," *IEEE Trans. Commun.*, vol. 68, no. 6, pp. 3808–3833, Jun. 2020.
- [6] D. Gottesman, "Stabilizer codes and quantum error correction," Ph.D. thesis, California Inst. Technol., Pasadena, CA, USA, 1997.
- [7] S. Shao, P. Hailes, T.-Y. Wang, J.-Y. Wu, R. G. Maunder, B. M. Al-Hashimi, and L. Hanzo, "Survey of turbo, LDPC, and polar decoder ASIC implementations," *IEEE Commun. Surveys Tuts.*, vol. 21, no. 3, pp. 2309–2333, 3rd Quart., 2019.
- [8] Z. B. Kaykac Egilmez, L. Xiang, R. G. Maunder, and L. Hanzo, "The development, operation and performance of the 5G polar codes," *IEEE Commun. Surveys Tuts.*, vol. 22, no. 1, pp. 96–122, 1st Quart., 2020.
- [9] V. Bioglio, C. Condo, and I. Land, "Design of polar codes in 5G new radio," *IEEE Commun. Surveys Tuts.*, vol. 23, no. 1, pp. 29–40, 1st Quart., 2021.
- [10] Y. Fang, Y. Bu, P. Chen, F. C. M. Lau, and S. A. Otaibi, "Irregular-mapped protograph LDPC-coded modulation: A bandwidth-efficient solution for 6G-enabled mobile networks," *IEEE Trans. Intell. Transp. Syst.*, vol. 24, no. 2, pp. 2060–2073, Feb. 2023.
- [11] J. M. Renes, F. Dupuis, and R. Renner, "Efficient polar coding of quantum information," *Phys. Rev. Lett.*, vol. 109, no. 5, Aug. 2012, Art. no. 050504.
- [12] Z. Babar, Z. B. Kaykac Egilmez, L. Xiang, D. Chandra, R. G. Maunder, S. X. Ng, and L. Hanzo, "Polar codes and their quantum-domain counterparts," *IEEE Commun. Surveys Tuts.*, vol. 22, no. 1, pp. 123–155, 1st Quart., 2020.
- [13] D. J. C. MacKay, G. Mitchison, and P. L. McFadden, "Sparse-graph codes for quantum error correction," *IEEE Trans. Inf. Theory*, vol. 50, no. 10, pp. 2315–2330, Oct. 2004.
- [14] Z. Babar, P. Botsinis, D. Alanis, S. X. Ng, and L. Hanzo, "Fifteen years of quantum LDPC coding and improved decoding strategies," *IEEE Access*, vol. 3, pp. 2492–2519, 2015.
- [15] D. Poulain, J.-P. Tillich, and H. Ollivier, "Quantum serial turbo codes," *IEEE Trans. Inf. Theory*, vol. 55, no. 6, pp. 2776–2798, Jun. 2009.
- [16] Z. Babar, P. Botsinis, D. Alanis, S. X. Ng, and L. Hanzo, "The road from classical to quantum codes: A hashing bound approaching design procedure," *IEEE Access*, vol. 3, pp. 146–176, 2015.
- [17] A. R. Calderbank, E. M. Rains, P. M. Shor, and N. J. A. Sloane, "Quantum error correction via codes over GF(4)," *IEEE Trans. Inf. Theory*, vol. 44, no. 4, pp. 1369–1387, Jul. 1998.
- [18] E. M. Rains, "Nonbinary quantum codes," *IEEE Trans. Inf. Theory*, vol. 45, no. 6, pp. 1827–1832, Sep. 1999.
- [19] F. R. Fernandes Pereira, G. G. La Guardia, and F. M. de Assis, "Classical and quantum convolutional codes derived from algebraic geometry codes," *IEEE Trans. Commun.*, vol. 67, no. 1, pp. 73–82, Jan. 2019.
- [20] Z. Babar, S. X. Ng, and L. Hanzo, "EXIT-chart-aided near-capacity quantum turbo code design," *IEEE Trans. Veh. Technol.*, vol. 64, no. 3, pp. 866–875, Mar. 2015.
- [21] Z. Babar, H. V. Nguyen, P. Botsinis, D. Alanis, D. Chandra, S. X. Ng, and L. Hanzo, "Serially concatenated unity-rate codes improve quantum codes without coding-rate reduction," *IEEE Commun. Lett.*, vol. 20, no. 10, pp. 1916–1919, Oct. 2016.
- [22] D. Chandra, Z. Babar, S. X. Ng, and L. Hanzo, "Near-hashing-bound multiple-rate quantum turbo short-block codes," *IEEE Access*, vol. 7, pp. 52712–52730, 2019.
- [23] S. T. Brink, "Convergence of iterative decoding," *Electron. Lett.*, vol. 35, no. 10, pp. 806–808, May 1999.
- [24] S. T. Brink, "Convergence behavior of iteratively decoded parallel concatenated codes," *IEEE Trans. Commun.*, vol. 49, no. 10, pp. 1727–1737, Oct. 2001.
- [25] M. Tuchler, "EXIT charts of irregular codes," in *Proc. Conf. Inf. Sci. Syst.*, 2002, pp. 748–753.
- [26] M. Tuchler, "Design of serially concatenated systems depending on the block length," *IEEE Trans. Commun.*, vol. 52, no. 2, pp. 209–218, Feb. 2004.
- [27] J. Kliewer, S. X. Ng, and L. Hanzo, "Efficient computation of EXIT functions for nonbinary iterative decoding," *IEEE Trans. Commun.*, vol. 54, no. 12, pp. 2133–2136, Dec. 2006.
- [28] M. El-Hajjar and L. Hanzo, "EXIT charts for system design and analysis," *IEEE Commun. Surveys Tuts.*, vol. 16, no. 1, pp. 127–153, 1st Quart., 2014.
- [29] S. Benedetto, D. Divsalar, G. Montorsi, and F. Pollara, "Serial concatenation of interleaved codes: Performance analysis, design, and iterative decoding," *IEEE Trans. Inf. Theory*, vol. 44, no. 3, pp. 909–926, May 1998.
- [30] I. Land, "Reliability information in channel decoding," Ph.D. thesis, Christian-Albrechts-Univ. Kiel, Kiel, Germany, 2005.
- [31] D. Chandra, Z. Babar, H. V. Nguyen, D. Alanis, P. Botsinis, S. X. Ng, and L. Hanzo, "Quantum coding bounds and a closed-form approximation of the minimum distance versus quantum coding rate," *IEEE Access*, vol. 5, pp. 11557–11581, 2017.
- [32] A. R. Calderbank and P. W. Shor, "Good quantum error-correcting codes exist," *Phys. Rev. A, Gen. Phys.*, vol. 54, no. 2, pp. 1098–1105, Aug. 1996.
- [33] A. R. Calderbank, E. M. Rains, P. W. Shor, and N. J. A. Sloane, "Quantum error correction and orthogonal geometry," *Phys. Rev. Lett.*, vol. 78, no. 3, pp. 405–408, Jan. 1997.
- [34] D. Chandra, Z. Babar, H. V. Nguyen, D. Alanis, P. Botsinis, S. X. Ng, and L. Hanzo, "Quantum topological error correction codes: The classical-to-quantum isomorphism perspective," *IEEE Access*, vol. 6, pp. 13729–13757, 2018.
- [35] P. Botsinis, Z. Babar, D. Alanis, D. Chandra, H. Nguyen, S. X. Ng, and L. Hanzo, "Quantum error correction protects quantum search algorithms against decoherence," *Sci. Rep.*, vol. 6, no. 1, pp. 1–13, Dec. 2016.
- [36] R. Cleve and D. Gottesman, "Efficient computations of encodings for quantum error correction," *Phys. Rev. A, Gen. Phys.*, vol. 56, no. 1, pp. 76–82, Jul. 1997.
- [37] J. Roffe, "Quantum error correction: An introductory guide," *Contemp. Phys.*, vol. 60, no. 3, pp. 226–245, Jul. 2019.
- [38] J. Hagenauer, "Rate-compatible punctured convolutional codes (RCPC codes) and their applications," *IEEE Trans. Commun.*, vol. COM-36, no. 4, pp. 389–400, Apr. 1988.
- [39] J. E. Martinez, P. M. Crespo, and J. Garcia-Frías, "On the performance of interleavers for quantum turbo codes," *Entropy*, vol. 21, no. 7, pp. 1–9, 2019.
- [40] M. A. Nielsen and I. L. Chuang, *Quantum Computation and Quantum Information*. Cambridge, U.K.: Cambridge Univ. Press, 2000.

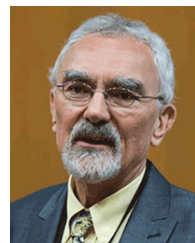
- [41] H. V. Nguyen, Z. Babar, D. Alanis, P. Botsinis, D. Chandra, S. X. Ng, and L. Hanzo, "EXIT-chart aided quantum code design improves the normalised throughput of realistic quantum devices," *IEEE Access*, vol. 4, pp. 10194–10209, 2016.
- [42] J. E. Martinez, P. Fuentes, P. M. Crespo, and J. Garcia-Frías, "Pauli channel online estimation protocol for quantum turbo codes," in *Proc. IEEE Int. Conf. Quantum Comput. Eng. (QCE)*, Oct. 2020, pp. 102–108.
- [43] J. E. Martinez, P. M. Crespo, and J. Garcia-Frías, "Depolarizing channel mismatch and estimation protocols for quantum turbo codes," *Entropy*, vol. 21, no. 12, pp. 1133–1147, 2019.
- [44] C. H. Bennett, D. P. D. Vincenzo, J. A. Smolin, and W. K. Wootters, "Mixed-state entanglement and quantum error correction," *Phys. Rev. A, Gen. Phys.*, vol. 54, no. 5, pp. 3824–3851, Nov. 1996.
- [45] M. M. Wilde, M.-H. Hsieh, and Z. Babar, "Entanglement-assisted quantum turbo codes," *IEEE Trans. Inf. Theory*, vol. 60, no. 2, pp. 1203–1222, Feb. 2014.
- [46] A. Banerjee, F. Vatta, B. Scanavino, and D. J. Costello, "Nonsystematic turbo codes," *IEEE Trans. Commun.*, vol. 53, no. 11, pp. 1841–1849, Nov. 2005.
- [47] M. Houshmand and M. M. Wilde, "Recursive quantum convolutional encoders are catastrophic: A simple proof," *IEEE Trans. Inf. Theory*, vol. 59, no. 10, pp. 6724–6731, Oct. 2013.
- [48] Y.-J. Wang, Z.-Y. Xiao, Y. Zhang, X.-Y. Xiong, and S. Shi, "Construction of multiple-rate quantum LDPC codes sharing one scalable stabilizer circuit," *IEEE Trans. Commun.*, vol. 71, no. 2, pp. 1071–1082, Feb. 2023.
- [49] S. Yang and R. Calderbank, "Quantum spatially-coupled codes," 2023, *arXiv:2305.00137*.
- [50] X.-J. Li, D. Pan, G.-L. Long, and L. Hanzo, "Single-photon-memory measurement-device-independent quantum secure direct communication—Part I: Its fundamentals and evolution," *IEEE Commun. Lett.*, vol. 27, no. 4, pp. 1055–1059, Apr. 2023.
- [51] X.-J. Li, D. Pan, G.-L. Long, and L. Hanzo, "Single-photon-memory measurement-device-independent quantum secure direct communication—Part II: A practical protocol and its secrecy capacity," *IEEE Commun. Lett.*, vol. 27, no. 4, pp. 1060–1064, Apr. 2023.
- [52] D. Chandra, A. S. Cacciapuoti, M. Caleffi, and L. Hanzo, "Direct quantum communications in the presence of realistic noisy entanglement," *IEEE Trans. Commun.*, vol. 70, no. 1, pp. 469–484, Jan. 2022.
- [53] D. Cruz, F. A. Monteiro, and B. C. Coutinho, "Quantum error correction via noise guessing decoding," 2022, *arXiv:2208.02744*.
- [54] D. Chandra, Z. B. Kaykac Egilmez, Y. Xiong, S. X. Ng, R. G. Maunder, and L. Hanzo, "Universal decoding of quantum stabilizer codes via classical guesswork," *IEEE Access*, vol. 11, pp. 19059–19072, 2023.



DARYUS CHANDRA received the B.Eng. and M.Eng. degrees in electrical engineering from Universitas Gadjah Mada, Indonesia, in 2013 and 2014, respectively, and the Ph.D. degree from the Next Generation Wireless Group, School of Electronics and Computer Science, University of Southampton, U.K., in 2020. He was a Postdoctoral Research Fellow with the Quantum Internet Research Group, University of Naples Federico II, Italy. Currently, he is a Postdoctoral Research Fellow with the Next Generation Wireless Group, School of Electronics and Computer Science, University of Southampton. His research interests include classical and quantum error-correction codes, quantum information, and quantum communications.



SOON XIN NG (Senior Member, IEEE) received the B.Eng. degree (Hons.) in electronic engineering and the Ph.D. degree in telecommunications from the University of Southampton, U.K., in 1999 and 2002, respectively. From 2003 to 2006, he was a Postdoctoral Research Fellow, working on collaborative European research projects, such as SCOUT, NEWCOM, and PHOENIX. Since August 2006, he has been a member of the Academic Staff with the School of Electronics and Computer Science, University of Southampton. He is currently a Professor of next generation communications with the University of Southampton. He has involved in OPTIMIX and CONCERTO European Projects and the IU-ATC and UC4G Projects. He was a Principal Investigator of an EPSRC Project on "Cooperative Classical and Quantum Communications Systems." His research interests include adaptive coded modulation, coded modulation, channel coding, space-time coding, joint source and channel coding, iterative detection, OFDM, MIMO, cooperative communications, distributed coding, quantum communications, quantum error correction codes, joint wireless-and-optical-fiber communications, game theory, artificial intelligence, and machine learning. He has published over 260 papers and coauthored two John Wiley/IEEE Press books in this field. He is a fellow of the Higher Education Academy, U.K., and a Chartered Engineer and a fellow of IET. He acted as the TPC/track/workshop chair for various conferences. He is one of the Founders and Officers of the IEEE Quantum Communications and Information Technology Emerging Technical Subcommittee (QCIT-ETC). He was the IEEE ComSoc Representative at the IEEE Nanotechnology Council (NTC), from 2020 to 2021. He was a Program Leader of Electrical and Electronic Engineering (EEE), from 2018 to 2021, and has been the ECS Doctoral Program Director with the University of Southampton, since 2021. He serves as an Editor of *Quantum Engineering*. He was a Guest Editor of the special issues in *IEEE JOURNAL ON SELECTED AREAS IN COMMUNICATION* and an Editor in *IEEE ACCESS* and the *KSII Transactions on Internet and Information Systems*.



LAJOS HANZO (Life Fellow, IEEE) received the master's and Ph.D. degrees from Technical University (TU) of Budapest, in 1976 and 1983, respectively, the D.Sc. degree from the University of Southampton, in 2004, and the joint Honorary Doctorate degrees from the TU of Budapest, in 2009, and the University of Edinburgh, in 2015. He has published more than 2000 contributions at IEEE Xplore and 19 Wiley-IEEE Press books and has helped the fast-track career of 123 Ph.D. students. Over 40 of them are professors at various stages of their careers in academia and many of them are leading scientists in the wireless industry. He is a fellow of the Royal Academy of Engineering (FREng), IET, and EURASIP. He is currently a Foreign Member of the Hungarian Academy of Sciences. He was a recipient of the 2022 Eric Sumner Field Award. He has served several terms as a Governor of both IEEE ComSoc and VTS. He is the former Editor-in-Chief of the IEEE Press.

...